

1 How is strain localized in a meta-granitoid, mid-crustal basement  
2 section? Spatial distribution of deformation in the central Aar  
3 massif (Switzerland)

4  
5 P. WEHRENS<sup>a,b</sup>, R. BAUMBERGER<sup>a,b</sup>, A. BERGER<sup>a</sup>, M. HERWEGH<sup>a\*</sup>

6  
7 <sup>a</sup> University of Bern, Institute of Geological Sciences, Baltzerstrasse 1+3, 3012 Bern, Switzerland

8  
9 <sup>b</sup> Federal Office of Topography, Swiss Geological Survey, Seftigenstrasse 264, 3084 Wabern, Switzerland

10  
11 \* Corresponding author, Institute of Geological Sciences, Baltzerstrasse 1+3, 3012 Bern, Switzerland.

12 Tel: +41(0)31 6314832

13 Email: marco.herwegh@geo.unibe.ch

14  
15 A. Berger: alfons.berger@geo.unibe.ch

16 M. Herwegh: marco.herwegh@geo.unibe.ch

17 R. Baumberger: roland.baumberger@swisstopo.ch

18  
19 Keywords: strain, localization, mid-crustal, shear zone, granitoid, Alpine

20

21

22

23

24

25 **Abstract**

26 This study investigates strain distribution in granitoid rocks formerly in the middle  
27 crust in the Central Aar massif, Switzerland and places the deformation behavior in the  
28 tectonic framework of the Alpine orogeny. Strain is heterogeneously distributed in terms  
29 of strain partitioning forming several hundreds of closely spaced shear zones (SZ) (>80  
30 SZ/km with SZ thicknesses <10 cm; about 10 SZ/km with SZ thicknesses of 0.5-10 m)  
31 separating 3D bodies of low to moderate background strain. Both the degree of  
32 background-strain intensity as well as the number of shear zones increases from granitic  
33 to granodioritic host rocks and is controlled by primary variations in the mica content  
34 between 10-15 vol% (granodiorite) and <8 vol% (granite). Shear zones evolved from  
35 ductile shearing in granodiorites, whereas they often nucleated from fractures in the  
36 stronger granites.

37 The majority of the steep shear zones preferentially accommodated upward motion  
38 by the southern Block leading to an increase in peak metamorphic conditions from 250°  
39 in the North to 450°C in the South of the Aar massif. The shear zones initiated at about  
40 18-20 km depths during a stage of crustal thickening (Handegg phase). Subsequent  
41 deformation reactivated some shear zones with a gradual transition from reverse dip-slip  
42 over oblique-slip to strike-slip shear zones under local transpressional conditions  
43 (Oberaar phase).

44

## 45 **1 Introduction**

46 The continental middle crust is mainly built up of polymetamorphic gneisses  
47 dissected by magmatic intrusions forming both compositional and mechanical  
48 anisotropies at a variety of scales. Therefore deformation tends to be distributed  
49 heterogeneously, depending on the effective material properties of the rock types and  
50 mechanical boundaries (e.g. Vernon and Flood, 1988). Deformation concentrated in  
51 domains with reduced rock strength is called strain localization, where ductile non-  
52 coaxial, high strain zones can evolve, which are referred to as shear zones. Information  
53 about the geometric, temporal and kinematic relationships of shear zones is essential in  
54 understanding finite strain, as well as the deformation history of orogens, thrusts and  
55 strike-slip zones (e.g., Ramsay, 1980; Choukroune and Gapais, 1983; Gapais et al., 1987;  
56 Marquer et al., 1996; Carreras et al., 2010; Menegon and Pennacchioni, 2010).

57 During nucleation and evolution of shear zones, two different end-members can be  
58 considered: (i) Rheology-dependent localization in a homogeneous material where no  
59 pre-existing mechanical anisotropy is present (Mancktelow, 2002), and (ii) reactivation of  
60 pre-existing mechanical anisotropies or discontinuities (Guermani and Pennacchioni,  
61 1998; Mancktelow and Pennacchioni, 2005; Pennacchioni, 2005). A current debate is  
62 whether such strain localization occurs entirely under viscous conditions (Platt and Behr,  
63 2011; Peters et al., 2016) or requires fractures that act as precursors for the subsequent  
64 ductile deformation (Mancktelow and Pennacchioni, 2005; Fousseis et al., 2006; Handy et  
65 al., 2007; Pennacchioni and Mancktelow, 2007). In the case of granitoid middle crust,  
66 relatively few studies have investigated the link between rock composition and  
67 mechanical anisotropies (e.g. Vernon and Flood, 1988; Wintsch et al., 2005). Particularly

68 the link between the quantitative characterization of strain patterns at the scale of meters  
69 versus several kilometers, as stated recently by Horsman et al. (2008) or Raynaud and  
70 Vasseur (2014), needs to be further investigated.

71 We investigate this problem by studying a large segment of exhumed mid-crustal  
72 basement rocks at different scales within a total volume of several cubic kilometers. The  
73 study area consists of metamorphic and igneous rocks of the Aar massif (southern  
74 Haslital, Central Switzerland), which underwent Alpine deformation. Combining field  
75 relationships with microstructural investigations, we address questions about how, where  
76 and when strain is localized at mid-crustal conditions including the evolution of  
77 subsequent exhumation.

## 78 **2 Geological setting**

79 The Aar massif belongs to the External Crystalline Massifs of the Alps and is mainly  
80 composed of Paleozoic basement gneisses and migmatites, which were intruded by  
81 Variscan and post-Variscan plutons associated with the evolution of Permo-  
82 Carboniferous half grabens (Figs. 1 and 2a, Labhart, 1977; Abrecht, 1994; Schaltegger,  
83 1994). Along the Haslital valley, four plutons can be identified (i.e. Mittagflue granite,  
84 Central Aar granite, Grimsel granodiorite and Southwestern Central Aar granite, Fig. 2a),  
85 which are all of Early Permian age (Schaltegger, 1990).

86 (INSERT FIGURE 1 HERE)

87 The pre-Variscan basement rocks are effected by multiple stages of deformation  
88 of Proterozoic, Ordovician, to Variscan and finally Alpine age (Stalder, 1964; Steck,  
89 1968; Labhart, 1977; Schaltegger, 1993; Schaltegger et al., 2003). In contrast, the post-

90 Variscan intrusives have only recorded Alpine deformation. For the Haslital, earlier  
91 research suggested an Alpine deformation gradient with both increasing deformation and  
92 metamorphism southward (Choukroune and Gapais, 1983; Bambauer et al., 2005;  
93 Bambauer et al., 2009). From the northern boundary (Innertkirchen) of the Aar massif to  
94 the south (Grimsel Pass), peak Alpine metamorphic conditions increase from lower to  
95 upper greenschist facies (Bambauer et al., 2005; Challandes et al., 2008; Bousquet, 2012;  
96 Goncalves et al., 2012). In light of the structural evolution, different deformation stages  
97 have been suggested for the southern margin of the Aar massif (Steck, 1968).

98 Northwest-directed Alpine thrusting (s1 and stage1, respectively, of Steck, 1968 and  
99 Rolland et al., 2009) led to development of localized high-strain shear zones isolating  
100 lenses of lesser deformation at a variety of scales. In granites of the southern part of the  
101 Haslital, this geometry was referred to as an anastomosing zone pattern (Choukroune and  
102 Gapais, 1983; Marquer et al., 1985; Gapais et al., 1987). Subsequently, this geometrical  
103 relationship has been used in many studies to geometrically describe mid-crustal shear  
104 zones.

105 P-T conditions of the main Alpine deformation in these shear zones reached a  
106 maximum temperature of 450 °C and pressure of 6.5 kbar (Goncalves et al., 2012)  
107 corresponding to depths of ~18-20 km. Deformation is dated at ~22-17 Ma (Challandes  
108 et al., 2008; Rolland et al., 2009) and 13.8-12.2 Ma (Rolland et al., 2009), for a first and a  
109 second stage of ductile shearing, respectively.

### 110 **3 Analytical Methods**

111 Our analysis of strain distribution in the Aar Massif along the Haslital transect  
112 involves a detailed study of large-scale (km), meso-scale (m to hundreds of m),  
113 handspecimen-scale (cm to dm) and micro-scale (mm) structures. A GIS-based remote-  
114 sensing structural map verified by fieldwork, served as the base map. Field relationships  
115 and microstructural investigations were used to determine the kinematics and relative  
116 ages of structures as well as to interpret the deformation processes.

117 To quantify the actual rock volume affected by high strain deformation, and to  
118 quantify the influence of compositional variations on subsurface deformation, data from  
119 the so-called “Transitgas-tunnel” (Schneider, 1974) were also gathered (Fig. 2). These  
120 data allow the unique investigation of the spatial and volumetric distribution of brittle and  
121 ductile strain in a continuous horizontal transect through a former mid-crustal section.  
122 Deformation intensity, as well as the distribution and dimensions (thicknesses) of  
123 mylonitic and cataclastic fault zones were quantified along this transect.

124 To qualitatively describe the degree of deformation on the outcrop scale, we used the  
125 foliation intensity, by means of optically visible spacing of sheet silicates and feldspars,  
126 in combination with the degree of grain size reduction. Here, the fabric of micas, quartz  
127 (size and elongation) and feldspars (size and elongation) was used. At a first glance,  
128 changes in foliation intensity and a decrease in grain size correlate directly with strain  
129 within a specific rock type, but more care is required when different rock types are  
130 compared with each other. We correlated weakly to moderately schistose rocks with very  
131 small to small strain intensity, which basically characterizes the background strain in the  
132 area. In such tectonites, feldspars have undergone only limited grain-size reduction often

133 retaining their original magmatic shape. In high strain zones, polymineralic proto-  
134 mylonitic to mylonitic/strongly schistose to ultramylonitic fabrics represent the transition  
135 from medium strain over high strain to very high strain, respectively. In these transitions,  
136 dramatic changes in shapes and sizes of the mineral grains occur. Particularly the  
137 feldspars show a macroscopically visible grain-size reduction and an increase in the grain  
138 aspect ratio. Also the quartz aggregates are strongly elongated due to ductile deformation.

139 We use the orientations of foliations, lineations and shear sense criteria for high-  
140 strain shear zones to infer the kinematic framework and its evolution during retrograde  
141 cooling and exhumation. Stretching lineations are mostly defined by elongated and  
142 dynamically recrystallized quartz aggregates that occur with synkinematic veins of  
143 unknown age. We infer that the stretching lineations on these aggregates represent the  
144 last increments of ductile strain before the fabric became frozen, rather than the finite  
145 strain from the complete deformation history.

## 146 **4 Results**

### 147 **4.1 Host rock fabric**

148 All formerly magmatic rocks were deformed and metamorphosed to a variable  
149 degree ductilely during Alpine deformation, often developing a pervasive gneissic  
150 foliation.

151

#### 152 4.1.1 Meta-plutonic rocks

153 The Mittagflue granite is the northernmost plutonic body (Fig. 2a).

154 Compositionally, the Mittagflue granite is a massive leucocratic granite. Magmatic

155 feldspars have mm to cm grain sizes, while interstitial quartz aggregates are in the mm-  
156 range. The biotite content is around 3 vol% (Schaltegger, 1989; Schaltegger, 1990) and  
157 the grain sizes are <5 mm. The Mittagflue granite has little to no internal foliation and is  
158 therefore rather isotropic, except at its contacts with neighboring rocks.

159 To the south, the Central Aar granite is the largest granitic body of the Aar massif and is  
160 located in the center of the massif (Fig. 2a). It has a crystallization age of around  $297 \pm 2$   
161 Ma (Schaltegger, 1989; Schaltegger, 1990; Schaltegger and Corfu, 1992). The CAGr has  
162 a similar biotite content (4-8 vol%) compared to the Mittagflue granite (Table 1, Fig. 3a).  
163 Feldspar grains, biotite grains and quartz aggregates have average sizes <2 cm, <0.5-1 cm  
164 and <0.3-0.5 cm, respectively. In most cases, the quartz is entirely dynamically  
165 recrystallized ( $\sim 150 \pm 50 \mu\text{m}$ ) by subgrain-rotation recrystallization owing to Alpine  
166 deformation. Additionally, the CAGr locally has primary magmatic features such as  
167 schlieren and mafic enclaves. Aligned magmatic feldspar grains, as well as a shape-  
168 preferred orientation of the elongated mafic enclaves, define a primary magmatic  
169 foliation, which mostly is parallel to the main NE-SW striking Alpine deformation. The  
170 CAGr is cut by late (post-Variscan) aplitic and meta-mafic dykes (Stalder, 1964;  
171 Schaltegger, 1990). Alpine background strain is characterized by the alignment of biotite  
172 and flattening of interstitial quartz leading to a weakly developed foliation (Fig. 3a).

173         The Grimsel granodiorite is located further south and is more intensely deformed  
174 toward the Grimsel Zone (Fig. 2a). Within error, the granodiorite has the same  
175 crystallization age as the CAGr (Schaltegger & Corfu 1992), as corroborated by the  
176 mingling structures of GrGr and CAGr related melts. Compositionally, the GrGr is  
177 markedly different from the CAGr because it has a greater biotite content of 12-15 vol%

178 (Table 1, Figs. 3c, 4a). Primary magmatic heterogeneity is stronger in the GrGr and  
179 characterized by mafic enclaves, compositional banding and schlieren. Similarly to the  
180 CAGr, the GrGr is also cut by aplitic and meta-mafic dykes (Fig. 3g). The grain sizes in  
181 domains least affected by Alpine deformation are for feldspars, biotite and dynamically  
182 recrystallized quartz, respectively, < 2 cm, < 0.5 mm and < 180  $\mu\text{m}$ . Furthermore, the  
183 GrGr has a boundary facies along its southern rim, which is defined by an aplitic granite  
184 with strong internal heterogeneity (Stalder, 1964; Dollinger, 1989; Schaltegger, 1990).  
185 The Alpine background strain is characterized by a variably developed foliation defined  
186 by aligned biotite, including locally developed augen-gneiss textures.

187 The Southwestern Aar granite is the southernmost intrusive rock along the  
188 Haslital transect, and equivalent in composition, microstructure as well as age to the  
189 CAGr (Fig. 2). To the south, the Southwestern Aar granite is in contact with the  
190 Ausserberg-Avat Zone (Stalder, 1964; Schaltegger, 1990). Alpine background strains  
191 generally define a weak foliation (Fig. 3i)

192

#### 193 4.1.2 Meta-dykes

194 Aplitic dykes occur more often within the GrGr than the CAGr. Their thicknesses  
195 range from cm to several meters. They have clear intrusive contacts and represent late-  
196 stage magmatic differentiation within the post-Variscan granitoids (Stalder, 1964;  
197 Schaltegger, 1994). The grain sizes of feldspars and quartz are < 3mm. The dykes are  
198 isotropic and have no internal foliation, and are dissected by an intense fracture network  
199 near Alpine high-strain zones.

200           Meta-mafic dykes are numerous in the study area and have partly been classified  
201 as meta-lamproids (Oberhänsli, 1986). The contacts between plutonic host rocks and  
202 meta-mafic dykes are clear and discrete. Compositionally, they are characterized by a  
203 high biotite content (up to 85 vol%, Table 1). The foliation is intense and the grain sizes  
204 of mica and feldspars are < 50 µm. If suitably oriented, the meta-mafic dykes belong to  
205 most intensely deformed rock type in the area (Fig. 3h). Some authors postulate that these  
206 meta-mafic dykes are unrelated to the post-Variscan granitoid emplacement (Oberhänsli,  
207 1986). However, meta-mafic and aplitic dikes show a geochemical correlation with the  
208 granitoids and crosscut the latter (Fig. 3g). Therefore, meta-mafic dykes as well as aplitic  
209 dykes are thought to be associated with the latest stages of post-Variscan granitoid  
210 emplacement (Schaltegger, 1989).

211

#### 212 4.1.3 Polymetamorphic gneisses

213           The Grimsel Zone (Fig. 2) is defined as the polymetamorphic basement rocks  
214 between the GrGr and the Southwestern Aar granite, and is also known as “Gneis-  
215 Schiefer-Zwischenzone” (e.g., Stalder, 1964) owing to its limited thickness of <1 km.  
216 Lithologically, the Grimsel Zone is quite heterogeneous, consisting of pre-Variscan  
217 metamorphic rocks (i.e., granitoid gneisses and schists, biotite schists, chlorite schists and  
218 augen-gneisses, meta-rhyolites). At Grimsel Pass, this zone separates the Southwestern  
219 Aar granite from the GrGr (Stalder, 1964; Dollinger, 1989; Abrecht, 1994), and contains a  
220 well-developed foliation. Alpine overprint as defined by a new Alpine foliation, shear bands,  
221 sheared and/or asymmetrically folded quartz veins as well as opening of young quartz  
222 clefts dominates, but locally relicts of less intensely overprinted structures are preserved,

223 containing a pre-Alpine foliation, which is folded by younger deformation stages (Fig.  
224 3e).

225 The pre-Variscan basement rocks of the Ausserberg-Avat Zone define the  
226 southern boundary of the crystalline Aar massif (Fig. 2). They are composed of augen-  
227 gneisses, titanite gneisses, porphyritic gneisses, biotite gneisses and migmatites (Stalder,  
228 1964; Niggli, 1965; Abrecht, 1994). Similarly to the Grimsel Zone, it is difficult to  
229 discriminate between pre-Variscan and Alpine deformation due to deformation intensity.  
230 (INSERT FIGURES 3, 4 AND 5 HERE)

## 231 **4.2 High strain zones**

232 In the Alpine high-strain zones, ductile and brittle faults both occur. The younger  
233 brittle faults contain cataclasites, fault gouges and occasionally fault breccias. A  
234 hydrothermal breccia is well-documented at the Grimsel Pass, and partially overprints  
235 ductile shear zones (Hofmann et al., 2004; Belgrano et al., 2016).

236 The ductile shear zones are easily distinguished from their host rocks by greater  
237 foliation intensity and much smaller grain size (Fig. 4). Particularly in the intrusive rocks,  
238 the original cm-sized magmatic grains are replaced by new grains with sizes of a few  
239 micrometers (5-10  $\mu\text{m}$ , Figs. 4, 5). Along with alignment of sheet silicates and  
240 compositional banding, well-foliated polymineralic mylonites and ultramylonites occur  
241 (Fig. 4). Counting of these shear zones and also cataclastic faults along 12 km of the  
242 Transitgas tunnel in the area between Rättrichsbodensee and Grimsel Pass yield 90-125  
243 deformation features per km in the plutonic rocks (Fig. 2b and 6b,c). The high-strain  
244 domains, such as cataclasites, mylonites and ultramylonites, range from discrete mm-  
245 wide shear zones up to tens of meter wide shear domains with strong strain gradients

246 traced toward the host rocks. The mm-wide shear zones are most abundant, but typically  
247 have limited lateral continuity.

248 The appearance of the high strain domains depends on the phyllosilicate content  
249 (Table 1 and Fig. 3). The number of shear zones and the volume of affected host rock  
250 increases toward large-scale lithological contacts, and most notably the contact between  
251 the GrGr and Grimsel Zone (Figs. 2a and 6a,c). Also, the 0.5-5 meter wide shear zones  
252 increase, from 4 per km to 13 per km to 60 per km from the CAGr to GrGr to Grimsel  
253 Zone, respectively (Fig. 6b). Note also that the cataclasites of the Transitgas tunnel  
254 mostly overprint mylonitic precursors (Fig. 5). The increase in number, density and  
255 thickness of shear zones correlates directly with an increase in mica content (from CAGr  
256 to GrGr to Grimsel Zone; Figs. 3 and 6). Furthermore, the volume of the high strain zones  
257 increases with greater sheet-silicate content (Table 1 and Figs. 3, 6c). Deformation zones  
258 with a limited thickness ( $<0.1$  m) on the other hand, dominate within the post-Variscan  
259 intrusives, and most notably within the CAGr (104 shear zones per km).

260

261 (INSERT FIGURE 6 HERE)

262

#### 263 *4.2.1 Alpine deformation structures*

264 In line with previous studies (Steck, 1968; Rolland et al., 2009), two major phases  
265 of localized ductile Alpine deformation can be distinguished by structural orientations  
266 (shear plane, stretching lineation), kinematics and crosscutting relationships for the shear  
267 zones. We named the two phases the Handegg- and Oberaar-phase after their respective  
268 type localities. Geometries and strike directions of the corresponding structures are very

269 consistent in the Aar massif and therefore have a regional significance (Figs. 7, 8). The  
270 older phase is named after the locality at Handegg (666'600/162'800), and is  
271 characterized by steeply oriented WSW-ENE striking narrow shear zones in the CAGr.  
272 The Oberaarsee (660'900/154'475) is the type locality for the younger deformation  
273 phase, where a wide system of major strike-slip shear zones of similar orientation is  
274 located.

275 (INSERT FIGURE 7 HERE)

#### 276 4.2.1.1 *Handegg phase*

277 Shear zones belonging to the Handegg phase are identified by their steep  
278 lineations (Fig. 2b, 7a, 8, supplementary material Figs. A-C, F). The structures  
279 dominantly strike NE-SW to ENE-WSW and dip steeply to the SE, parallel to the  
280 foliation in the weakly deformed granitic host rocks. The structures show rather  
281 consistent orientations in all domains, except for the Ausserberg-Avat Zone where the  
282 shear zones dip steeply towards the NW (Figs. 2b, 8). Variations in dip allow the  
283 identification of two sets of shear zones: (i) A major set with dip angles of 65-80° shows  
284 reverse sense of shear and (ii) a second set with even steeper dips (80-90°) forming  
285 branches that interconnect the major zones (anastomosing shear zones of Choukroune and  
286 Gapais, 1983, see also supplementary material Figs. A-C) showing shear senses typical  
287 for normal faulting. The number of Handegg-phase shear zones (thickness 0.1-0.5 m)  
288 increases from the CAGr to the GrGr, while their spacing decreases, indicating  
289 progressive localization of deformation (Figs. 6a, 7a). Stretching lineations are mostly  
290 restricted to synkinematic quartz veins, which were affected by dynamic recrystallization.  
291 Within the Grimsel Zone (Fig. 7a), later dextral overprinting by the younger Oberaar-

292 phase deformation is pervasive and therefore Handegg-phase shear zones are not  
293 identifiable anymore (Fig. 7b).

294

#### 295 4.2.1.2 *Oberaar phase*

296 The Oberaar phase is dominantly characterized by slightly to moderately east  
297 plunging stretching lineations in dynamically recrystallized vein quartz on steeply south-  
298 dipping shear planes, indicating dextral oblique- to strike-slip movements (Figs. 2, 7b, 8,  
299 supplementary material Figs. D,E,F). Particularly towards the south, a small number of  
300 slightly SW to W plunging lineations exist (Fig. 8). Generally, the shear planes have a  
301 wide range of strikes from NNE-SSW, E-W to NW-SE (Fig. 9). Cross-cutting relations  
302 clearly show that the Oberaar phase structures dissect the Handegg phase structures (Figs.  
303 7a see white arrows; 9a,b; 9e,f; supplementary material Figs. D,E) indicating therefore a  
304 younger activity, which was previously observed (Steck 1968; Roland et al. 2009). Based  
305 on geometric orientations, the Oberaar-phase shear zones can be further subdivided into:  
306 (a) ENE-WSW striking Oberaar<sub>a</sub> orientation; (b) NW-SE striking Oberaar<sub>b</sub> orientation  
307 and (c) NE-SW striking Oberaar<sub>c</sub> orientation strike-slip shear zones (Fig. 7b).

308 Oberaar<sub>a</sub> shear zones dip steeply towards the SE and strike ENE-WSW (Figs. 7b,  
309 9b, supplementary material Fig. D). Commonly they are intensely foliated and have shear  
310 bands indicating a dextral sense of shear. Occasionally, E-W to NW-SE striking C'  
311 planes are developed, comparable in orientation to the Oberaar<sub>b</sub> structures (Fig. 9a,b).  
312 (INSERT FIGURE 9 HERE)

313 High strain domains related to the Oberaar<sub>a</sub> orientation run along the lithological  
314 contact between the GrGr and Grimsel Zone (SZ10 in Table 3; Fig. 7b) and between the

315 Grimsel Zone and the Southwestern Aar granite (SZ12 in Table 3; Fig. 7b). The Oberaar<sub>a</sub>  
316 orientation is dominant within the Grimsel Zone. Detailed mapping at the western end of  
317 Oberaarsee and the analysis of a N-S section across the Grimsel Pass shear zone (GPSZ;  
318 supplemental material Fig. F) demonstrates the rotation of the old NE-SW striking  
319 Handegg-phase foliation (with steep SE down dip lineations) from the rim into the  
320 younger ENE-WSW striking shear plane of one branch of the GPSZ related to the  
321 Oberaar phase. Note the changes in lineations from down dip to moderate SE plunging  
322 into subhorizontal orientation (Fig. 10; see also supplementary material Fig. B(b) and Fig.  
323 F). The rotation of both foliation and lineation, as well as the dextral shear sense  
324 indicators in the GPSZ, such as dextral C' structures, asymmetric folds and sheared old  
325 quartz veins as well as young open quartz clefts (Fig. 10), all support a dextral oblique to  
326 strike-slip shearing along the GPSZ (Fig. 10). Note that the range in plunges is also  
327 visible for the Oberaar lineations found across the entire study area, and also includes a  
328 few additional slight to moderately SW plunging ones (Figs. 2 and 8).

329 Steeply SW to S dipping and NW-SE to E-W striking Oberaar<sub>b</sub> shear zones are  
330 most common in the CAGr (Figs. 2 and 7b, 8). They have a dextral sense of shear, are  
331 mostly quite thin (few cm to dm) and clearly crosscut Handegg phase (Fig. 9).  
332 Crosscutting relationships with the Oberaar<sub>a</sub> shear zones are contradictory at different  
333 scales. While km-scale Oberaar<sub>b</sub> shear zones rotate into the large-scale Oberaar<sub>a</sub> shear  
334 zones of the Grimsel Zone (e.g. sz9 and others in Fig. 7b) and do not crosscut the latter,  
335 at the outcrop-scale smaller Oberaar<sub>b</sub> shear zones crosscut at some locations Oberaar<sub>a</sub>  
336 shear zones. In both cases, however, mylonitic shear zones evolved, which show an  
337 identical mineral paragenesis with stable chlorite and white mica but unstable biotite.

338 Oberaar phase shear zones occasionally exploit meta-mafic dykes or run along aplitic  
339 dykes. They have similar orientations to C' structures developed in Oberaar<sub>a</sub> shear zones.  
340 The lineations are dominantly slightly E-ENE plunging, but in few cases slight to  
341 moderately W-NW plunging. This geometry indicates an oblique slip movement with a  
342 strong dominant horizontal component of shear.

343 (INSERT FIGURE 10 HERE)

344 The third orientation (Oberaar<sub>c</sub>) of Oberaar shear zones is characterized by a set of  
345 sinistral shear zones (Figures 2, 3, 7 and 8). Overall, these shear zones strike NNE-SSW  
346 and dip steeply eastwards, but have a limited lateral continuity (Fig. 7b). Furthermore,  
347 their thicknesses do not exceed several tens of cm. They are best preserved in the more  
348 leucocratic rocks, i.e. CAGr and Southwestern Aar granite, although minor Oberaar<sub>c</sub>  
349 zones (thickness < 0.15 m) can also be found within the Grimsel Zone. Given that the  
350 number of these shear zones is rather limited and only very few lineations are found also  
351 point toward a slight oblique slip component (Figs. 2, 8). The mineral stabilities are  
352 identical to those of Oberaar<sub>a</sub> and Oberaar<sub>b</sub> shear zones.

353

#### 354 *4.2.2 Microstructural characterization*

355 The pre-Alpine (i.e., magmatic) microstructures of the post-Variscan intrusives  
356 consist of large-sized feldspar grains (plagioclase, K-feldspar), biotite and interstitial  
357 quartz. Often a planar fabric consisting of elongated feldspar grains due to magmatic flow  
358 is present (Fig. 11a,b).

359 (INSERT FIGURE 11 HERE)

360 In granitoid domains weakly affected by Alpine deformation, feldspar grains still  
361 retain their magmatic appearance (Fig. 11a). As a consequence of Alpine overprinting,  
362 grain size reduction occurs, where feldspar grains become fragmented by brittle  
363 deformation, together with precipitation of new fine-grained K-feldspar and albite.  
364 Interstitial quartz domains between magmatic feldspars become elongated due to  
365 deformation by intracrystalline plasticity and dynamic recrystallization by subgrain  
366 rotation recrystallization (compare Fig. 11b with 11 d,f). Furthermore, biotite is aligned  
367 subparallel to the macroscopic shear plane (Fig. 11c-f). Occasionally, epidote-filled veins  
368 parallel to the shear plane cut through the magmatic feldspar clasts and recrystallized  
369 quartz aggregates. Along these epidote-filled fractures, ductile micro-shear zones, defined  
370 by quartz and biotite recrystallization, develop (Wehrens et al., in press). With increasing  
371 strain, further grain size reduction accompanied by an increase in mica content is visible.

372 The Handegg-phase shear zones with the steep lineations, and located within the  
373 granites, are mm to several meter thick dark bands of strongly foliated to very fine-  
374 grained mylonitic to ultramylonitic rocks (Fig. 11c,d). The ultramylonitic domains consist  
375 of monomineralic, elongated quartz aggregates (hundreds of  $\mu\text{m}$  wide) and polymineralic  
376 bands (ranging from several  $\mu\text{m}$  up to cm wide, Fig. 11d). Quartz aggregates were  
377 dominantly recrystallized by subgrain rotation recrystallization (Table 4, Fig. 11b).  
378 Recrystallized quartz grain sizes range from 50-200  $\mu\text{m}$ . Polymineralic bands are  
379 characterized by recrystallized K-feldspar, albite, epidote, quartz, biotite and white mica  
380 (Fig. 11d). Pinning of the boundaries of recrystallized grains leads to even smaller grain  
381 sizes (5-50  $\mu\text{m}$ ), compared to those of monomineralic quartz aggregates (Fig. 11d). Some

382 feldspar grains occur as porphyroclasts, while others undergo grain size reduction, which  
383 leads to grain sizes of 500 to 50  $\mu\text{m}$ .

384 Numerous shear zones from the Oberaar phase within the Grimsel Zone have mineral  
385 assemblages comparable to Handegg phase (Fig. 11e,f, Table 4). The Oberaar-phase  
386 shear zones within the post-Variscan intrusive rocks locally increase white mica content  
387 toward shear-zone centers, creating interconnected bands of pure but extremely fine-  
388 grained newly crystallized white mica (Fig. 11h).

389 Biotite is occasionally replaced by chlorite in rim regions of such shear zones.  
390 Biotite-stable conditions are present during both deformation stages. However,  
391 retrogression, and the associated reaction of biotite to chlorite, is restricted to the  
392 Oberaar-phase shear zones. Also, the appearance of white mica-rich domains result from  
393 retrograde mineral assemblages (Fig. 11 g,h). The retrograde mineral assemblage in the  
394 Oberaar phase-related microstructures is of lower temperature nature (Table 3).

## 395 **5 Discussion**

396 Our work demonstrates that deformation at mid-crustal levels, as observed at the  
397 southern rim of the Aar massif, is characterized by a rather heterogeneous and complex  
398 strain pattern, which is highly scale dependent (Fig. 12). This pattern provides  
399 information about the roles of compositional and mechanical anisotropies in the  
400 deformation of mid-crustal basement rocks. The observed pattern is a result of a  
401 combination of pre-Alpine anisotropies, changes in the kinematic framework, strain  
402 localization processes, and shear zone evolution. In this light, variations in the large-scale

403 background strain in host rocks must be distinguished from highly localized strain in  
404 shear zones (Figs. 3, 12, 13).

405

## 406 **5.1 Alpine kinematic evolution**

407 In the literature, two end-member concepts for the structural evolution of the  
408 internal deformation of the Central Aar massif have been discussed: (i) The bulk coaxial  
409 shortening model, where structures evolve during a single major deformation event  
410 (Choukroune and Gapais, 1983; Gapais et al., 1987); and (ii) multiphase deformation  
411 where different events occur sequentially in time (Steck, 1968; Rolland et al., 2009;  
412 Table 2). Studies favoring (i) were conducted in the central to northern part of the study  
413 area only (CAGr-GrGr of Fig. 2), missing the important large-scale strike-slip structures  
414 that occur along the Grimsel Pass shear zone (GPSZ) in the south (Figs. 2, 8,  
415 supplementary material Fig. F). (ii) Along with this unintended omission, a number of  
416 data sources support an interpretation involving multiphase deformation, including cross-  
417 cutting relationships (Figs. 2, 7, 9 and supplemental material Figs. B-F), different  
418 radiometric ages (Challandes et al., 2008; Rolland et al., 2009; Wehrens 2015) and a  
419 change in kinematics (Steck, 1968; Rolland et al., 2009), which facilitate the recognition  
420 of the Handegg and Oberaar phase cross-cutting relations indicate a clearly younger  
421 relative age of the Oberaar strike-slip structures compared to Handegg reverse and  
422 normal faulting (Figs. 9, supplemental material Figs. B-F, Table 2). Recent radiometric  
423 dating on neocrystallized mica corroborate at least a two-step deformation: ~22-17 Ma  
424 (Challandes et al., 2008; Rolland et al., 2009) and 13.8-12.2 Ma (Rolland et al., 2009),  
425 which we correlate with the Handegg and Oberaar phase, respectively (see locations of

426 radiometric ages in Fig. 7). The change from biotite-stable metamorphic conditions ( $T >$   
427  $400^{\circ}\text{C}$ ) of the Handegg structures to retrogressive mineralogical suites (e.g., chlorite and  
428 white mica stable, biotite unstable) of the Oberaar strike-slip shear zones also favor more  
429 than one deformation event. Last but not least, deformation further localized under cooler  
430 deformation conditions, forming the large-scale dextral Grimsel Pass strike-slip fault  
431 zone with the hydrothermally active Grimsel Breccia Zone in its core (Belgrano et al.,  
432 2016).

433 Collectively, these facts favor a multi-event deformation history, which is the  
434 tectonic scenario that we adopt for our analysis (Fig. 12). The gradually increasing  
435 metamorphic grade southward in the Haslital results from reverse shearing along the  
436 steeply S-dipping Handegg-phase shear zones. In general, these shear zones uplifted the  
437 southern hangingwall block exhuming rocks of higher metamorphic rocks (Fig. 12b). The  
438 accumulations of these south block up movements result in the nowadays exposed  
439 increasing in metamorphic grade from north to south.

440 The occurrence of reverse and normal faulting, respectively, along the major faults  
441 and the secondary branches (Figs. 13, supplementary material Figs. B,C,F) indicates the  
442 existence of a conjugate set, with preferential South block up movements as inferred by  
443 the dominance of reverse faults. Despite this clear geometric relationship in key outcrops,  
444 it might therefor be confusing to find similar shear plane orientations with normal and  
445 reverse shear senses (e.g. Fig. 8 see GrGr). Two different effects may cause this apparent  
446 discrepancy: (i) Progressive change in the major shear-zone orientation from steeply  
447 south dipping towards steeply north dipping from N to S (cf. Fig. 8 GrGr to AAZ). In the  
448 latter case, also the secondary branches will change their orientation yielding in

449 aforementioned overlap in shear plane orientations with opposing senses of shear. (ii)  
450 Passive rotation of the conjugate set of shear zones and reduction in the acute angle  
451 between them owing to horizontal shortening during Alpine compression.

452 (INSERT FIGURE 13 HERE)

453 The onset of the Oberaar phase had a clear change in kinematics, involving  
454 increased strain localization with greater strain partitioning. These changes might either  
455 have occurred abruptly or gradually. We observe rotations of the originally steeply south-  
456 plunging lineation, through a moderately E plunge, into a slightly E plunging to  
457 subhorizontal orientation (Figs. 2b, 7). This geometry is nicely reflected in the case of the  
458 strike-slip shear zone at Oberaarsee (Figs. 2, 10 and sz10 in Fig. 7b as well as in  
459 supplementary material Figs. B(b), F), where the rotation of the lineation is documented  
460 from the older high temperature parts preserved in the rim of the shear zones (lineations  
461 plunge from 69-58°) towards the young low temperature center of the shear zones  
462 (lineations plunging between 32-13° towards the ENE).

463 Despite some apparently contradicting cross-cutting relationships stated above, we  
464 suggest that the three orientations of the Oberaar-phase shear zones ( $SZ_{Oa}$ ,  $SZ_{Ob}$ ,  $SZ_{Oc}$ )  
465 were simultaneously active within the same kinematic framework: First, the km-scale  
466 shear zones show no cross-cutting relationship. Instead Oberaar<sub>b</sub> shear zones rotate into  
467 Oberaar<sub>a</sub> ones (Fig. 7b, Sz9 and Sz10). Second, they all formed mylonites with the same  
468 stable mineral assemblage, pointing to similar metamorphic conditions during ductile  
469 shearing. Third, they all show strong strike-slip/oblique-slip components, which contrast  
470 the Handegg structures and are typical for the Oberaar phase related shear zones (Figs. 2,  
471 7, see also Steck, 1968; Rolland et al., 2009). The dextral ENE-WSW striking major

472 strike-slip shear planes show similar orientations as shear zones from the Handegg phase  
473 (Fig. 13). Based on these observations, we suggest a formation of the three Oberaar  
474 orientations within the same kinematic framework, and interpret the dextral E-W to ENE-  
475 WSW shear zones and the sinistral NE-SW shear zones, respectively, to represent anti-  
476 and synthetic Riedel shear orientations (Fig. 13b). Hence the different strike-slip  
477 orientations belong to the same kinematic regime and can be attributed to an overall  
478 dextral transpressional framework (see also model of Carreras et al., 2010) with  
479 simultaneous activity. The apparently contradicting cross-cutting relationships at the  
480 outcrop-scale might therefore reflect local relative incremental activities of individual  
481 decameter-scale Oberaar<sub>o</sub> shear zones during the overall transpressive movements. In  
482 fact, the formation, slight rotation and deactivation of local shear zones is typical for non-  
483 coaxial shearing of Riedel systems.

## 484 **5.2 Effect of pre-Alpine anisotropies on Alpine deformation**

485 Generally, a considerable number of pre-Alpine material anisotropies served as  
486 nucleation sites for Alpine deformation. They include: i) compositional variations in the  
487 meta-magmatic rocks; ii) lithological contacts; and iii) pre-Alpine deformation fabrics  
488 (Fig. 12a).

489 i) Most important are original compositional variations in former magmatic  
490 rocks (Figs. 3, 12). Particularly variations in the amount of potential  
491 ‘mechanically weak’ phases, such as quartz and mica (e.g., Vernon and Flood,  
492 1988) combine with the dimension of the corresponding magmatic body to  
493 directly affect the degree and scale of Alpine deformational overprint (Fig.  
494 12). Deformation in the large-scale plutons has to be distinguished from that

495 in the smaller magmatic dikes (aplites, metamafic dikes). The volumetrically  
496 prominent CAGr and SWAGr with their weakly schistose fabrics, contain a  
497 modest general background strain compared to the moderately schistose and  
498 more mafic GrGr (Figs. 3, 12b, Table 1). Since the peak-Alpine metamorphic  
499 grade is nearly identical within all three intrusive rock types (450°C), it is the  
500 only slightly enhanced mica content of the GrGr (10-15 vol%), compared to  
501 that of CAGr/SWAGr (4-8 vol%), which forces the latter to behave more  
502 rigidly and allows concentration of deformation in the GrGr (Figs. 3, 12b).  
503 Note that this compositional variation also seems to affect the nucleation of  
504 shear zones either via ductile shearing (GrGr) or brittle fracturing  
505 (CAGr/SWAGr, see Wehrens et al. in press).

506 A similar compositional effect related to the sheet-silicate-content also  
507 accounts for the opposing deformation behavior of mafic and aplitic dikes  
508 (Figs. 3g,h; 12b, supplementary material Fig. E). Associated with the largest  
509 mica content in the study area (mica > 50 vol%), meta-mafic dykes generally  
510 have a strong internal foliation and invariably acted as Alpine ductile shear  
511 zones, when suitably oriented for shearing (Fig. 3g,h, supplementary material  
512 Fig. E(b)). If unfavorably oriented, host-rock-related shear zones crosscut the  
513 dykes (supplementary material Fig. E(a)), generating a new internal foliation  
514 for the dyke, which is parallel to the shear plane (e.g., SZ 7, Fig. 7b). On the  
515 other hand, aplitic dykes have the smallest mica contents (< 2 vol%) and  
516 developed biotite coated fracture networks when suitably oriented for  
517 shearing, but have almost no internal foliation (Fig. 3g). Instead, deformation

518 is always localized within the host rock adjacent to the aplite contact (SZ8,  
519 Figs. 7b and 9e,f). Similar observations have been made from the Tauern  
520 window (Pennacchioni and Mancktelow, 2007).

521 ii) Large-scale high-strain zones, whose thicknesses range from one meter to  
522 several tens of meters, occur along lithological boundaries between post-  
523 Variscan intrusives and pre-Variscan basement. These zones are the  
524 boundaries between the GrGr and Grimsel Zone (e.g. SZ10, Fig. b) and  
525 between the Grimsel Zone and Southwestern Aar granite (e.g. SZ12, Fig. b).

526 iii) Within the pre-Variscan basement of the Grimsel Zone, an axial planar  
527 foliation can occasionally be found that is cut by aplitic bodies related to the  
528 granite intrusion. Therefore, this foliation has a pre-Variscan origin (SZ10, 9).  
529 The remnants of pre-Alpine folds with axial plane foliation in the shear zones  
530 of the Grimsel Zone might also be an indicator of a long lasting deformation  
531 (Bell, 1978; Alsop and Holdsworth, 2002; Carreras et al., 2010), involving a  
532 possible pre-Alpine shear component. Note that this pre-existing planar fabric  
533 was reactivated during both the Alpine Handegg and Oberaar phases of  
534 deformation.

535

## 536 **5.3 Alpine strain localization**

### 537 *5.3.1 Initial Alpine strain localization*

538 Two end-member nucleation sites for strain localization are recognized in the  
539 study (Fig. 12): (i) nucleation along pre-existing mechanical anisotropies (Figs. 4, 12) and  
540 (ii) formation of new anisotropies by brittle failure (Figs. 5, 12b,c). (i) In terms of

541 initiation of Alpine shear zones, many important structures that have large thickness and  
542 lateral continuity result from reactivation of pre-existing mechanical anisotropies, or  
543 structural discontinuities that either evolved out of a lithological contact (e.g. GrGr -  
544 Grimsel Zone contact, Figs. 6, 7, 12a), compositional heterogeneity, or an earlier  
545 deformation event (Fig. 10). The sheared domains within the Grimsel Zone, for example,  
546 have a protracted long-lasting multistage reactivation history. Here, a (pre-) Variscan  
547 structure served as a km-scale mid-crustal mechanical anisotropy already present during  
548 emplacement of post-Variscan intrusions. Particularly, the intrusion and crystallization of  
549 the aplitic boundary facies and the Southwestern Aar granite generated isotropic host  
550 rocks with very small sheet-silicate content. Consequently, a considerable contrast in  
551 effective viscosity evolved between these mechanically stiffer plutonic rocks and the  
552 weaker, sheet-silicate-rich gneisses of the Grimsel Zone. Similar contrasts within the  
553 post-Variscan intrusives (i.e., meta-mafic dykes, aplitic dykes) induced localization of  
554 ductile strain as long as their orientations were appropriate for reactivation within the  
555 regional kinematic framework (Fig. 12a, 13). Especially around the Rättrichsbodensee, the  
556 pronounced occurrence of meta-mafic dykes at the transition from CAGr to GrGr caused  
557 strain to localize along these mechanically weaker magmatic precursors. Deformation  
558 reactivated such contacts during the Alpine orogeny.

559         In general, the sheet-silicate content and spatial distribution of sheet-silicate-rich  
560 rocks was crucial for controlling the intensity distribution of Alpine deformation in high  
561 strain domains, as well as for the background strain in weakly deformed domains of much  
562 of the host rocks (Fig. 12a). Sheet-silicate-rich lithologies like the Grimsel Zone, GrGr  
563 and meta-mafic dykes have a strong internal ductile deformation characterized by a

564 greater density and thickness of Handegg phase high-strain domains, compared to the  
565 more isotropic granitic rocks with a smaller sheet-silicate content (Figs. 6, 7 and 12).  
566 Besides the changes in high strain shearing, the higher sheet-silicate content in the GrGr  
567 also resulted in a larger amount of background strain in the GrGr, compared to the CAGr.  
568 This influence is illustrated by the higher proportion of strongly schistose fabrics within  
569 the GrGr (Figs. 3, 12b,c).

570 (ii) In contrast to type (i) shear zones within the isotropic parts of the post-  
571 Variscan plutons, shear zones with small sheet-silicate content are very discrete and thin  
572 (<0.1 m). They are occasionally several km in length, dissecting the granitic bodies in a  
573 regular planar manner. Given their large length to thickness ratio, combined with their  
574 straight planar geometries, we infer that these shear zones must have nucleated on pre-  
575 existing brittle fractures under semi brittle-ductile conditions. Additional evidence for  
576 brittle deformation at elevated temperature in this ductile deformation regime is found in  
577 biotite-bearing fracture coatings and epidote veins, which are overprinted by biotite- and  
578 white mica-bearing ductile shear zones (see also Wehrens et al., in press). Figure 5a-c  
579 documents such an overprinting sequence, comprising an initially formed network of  
580 biotite-coated fractures, which was overprinted by an ultramylonite. Such ultramylonites  
581 often widen and terminate in brittle horse-tail structures (Fig. 5c), providing further  
582 evidence for brittle structures acting as precursors for ductile shearing in the case of the  
583 CAGr (see also Wehrens 2015).

584 The idea of brittle precursors for the nucleation of granitic shear zones deformed  
585 under greenschist or amphibolite facies metamorphic conditions has been suggested by  
586 several authors (Segall and Simpson, 1986; Mancktelow and Pennacchioni, 2005; Füsseis

587 et al., 2006; Handy et al., 2007; Pennacchioni and Mancktelow, 2007; Fousseis and Handy,  
588 2008). In the case of our mid-crustal rock suite of granitoid origin, we infer that the  
589 fracture-induced nucleation of ductile shear zones is of particular importance in the  
590 isotropic sheet-silicate poor plutonic bodies already active during the Handegg phase  
591 (Figs. 12b and 13). With progressive shortening, they were probably steepened and  
592 reactivated as Oberaar<sub>a</sub> strike-slip shear zones. In contrast, Oberaar<sub>b,c</sub> orientations with  
593 their opposing shear senses, represent a simultaneously active conjugate set, which was  
594 newly formed during Oberaar<sub>a</sub> shearing. Despite their clear ductile deformation style, the  
595 similarity in geometry and kinematics to syn- and antithetic Riedel shear zones is  
596 appealing, provoking us to also postulate a brittle origin for the ductile Oberaar<sub>b</sub> phase  
597 and Oberaar<sub>c</sub> phase shear zones (Fig. 13b). Similar correlations between brittle and  
598 ductile features in shear band formation have previously been proposed (Shimamoto,  
599 1989). Note that all three Oberaar phase shear-zone orientations were reactivated during  
600 retrograde deformation as brittle faults representing important pathways for the  
601 circulation of hydrothermal fluids (Belgrano et al., 2016).

602

### 603 *5.3.2 Evolution of strain gradients*

604 Following from the two types of nucleation sites for ductile shearing (sheet-silicate  
605 content and fracture-induced mechanical anisotropy), the evolution of strain gradients has  
606 to be considered.

607 i) During ongoing deformation of ductile shear zones (i.e., sheet-silicate-rich zones),  
608 grain-size reduction induces strain localization (Fig. 12b,c). Meter-wide strain  
609 gradients formed from a weakly to moderately deformed rim towards a mylonitic

610 central zone and an ultramylonitic shear zone core. Hence, typical shear zone  
611 narrowing occurs (e.g., Means, 1995; Ebert et al., 2007; Herwegh et al., 2008;  
612 Haertel and Herwegh, 2014, Herwegh et al., 2016). Monomineralic quartz domains  
613 in the shear zone center are deformed by dislocation-creep processes, as they have  
614 strong crystallographic preferred orientation (CPO) correlated with textures related to  
615 subgrain rotation recrystallization in the fine-grained domains. The even smaller, 5 to  
616 50  $\mu\text{m}$ , recrystallized grain size combined with the equiaxed grain shapes and the  
617 absence of CPO within polymineralic domains suggest viscous granular flow as the  
618 dominant deformation mechanism (e.g., Stünitz and Fitz Gerald, 1993; Paterson,  
619 1995; Herwegh et al., 2011).

620 ii) In contrast, shear zones, which nucleated along fractures and are characterized by  
621 discrete narrow, high strain zones, must have widened after initial fracturing (Fig.  
622 12b,c). Fracturing at the grain scale results in a grain size decrease, dilatancy and an  
623 increase in reactive surface area. These preconditions promote fluid infiltration, mass  
624 transfer processes and mineral reactions. As a consequence, new sheet silicates  
625 crystallize and the proportion of these mechanically weak phases increases in the  
626 shear zones.

627 In this way, the effective viscosity of type (ii) shear zones converges toward that of  
628 type (i) shear zones by a reaction-weakening process (Fig. 12c). Nevertheless, major  
629 differences exist in the thicknesses of the two contrasting types of strain localization.  
630 Besides finite strain, in (i), the dimensions of the original compositional heterogeneities  
631 substantially influences the thickness of the high strain zones, while in (ii), the reaction  
632 progress and amount of fluid are the controlling parameters (see Wehrens et al., in press).

633 During retrograde deformation, shear zones further narrowed within sheet-silicate-  
634 rich domains (Figs. 11h and 12c). The local evolution of sheet-silicate-rich domains is  
635 most likely a combined effect of producing white mica and chlorite during ongoing  
636 cooling and synkinematic infiltration of fluids and precipitation of white mica. With  
637 progressive cooling, brittle deformation increases, finally leading to the formation of  
638 cataclastic zones and brittle fault gouges (Fig. 5d,e). Note that these gouges are not  
639 preserved at surface outcrops, but can be frequently found in drill cores from the  
640 underground tunnels (Wehrens et al., in press). Here, they mostly evolved out of ductile  
641 shear zones suggesting continuous strain localization with progressive cooling. Sheet-  
642 silicate-rich shear zones may develop under varying metamorphic conditions as indicated  
643 by previously published examples of shear zones with locally different compositions  
644 (Oliot et al., 2010; Goncalves et al., 2012).

645 (INSERT FIGURE 12 HERE)

646

### 647 *5.3.3 Meso-scale deformation*

648 On the small scale, individual shear zones are described in terms of their  
649 localization history, from initiation to final expression. On a larger scale, a mid-crustal  
650 section of several km is characterized by a particular distribution of such shear zones.  
651 Surface mapping (Fig. ) as well as subsurface quantification of deformation along the  
652 “Transitgas-tunnel” (Fig. 6) allowed for determination of the most important factors  
653 contributing to the km-scale strain distribution. This mid-crustal section is characterized  
654 by a multitude of shear zones ranging from mm to meters thickness (90-125 shear zones  
655 per km). Similar dimensions of shear-zone thicknesses and shear-zone spacings were

656 found in the Mont Blanc Massif (Rossi et al., 2005; Rolland et al., 2008). In the Aar  
657 massif, the strain distribution indicates an increase of deformation towards lithological  
658 contacts (Fig. 6a). Furthermore, a relationship between the deformation intensity and  
659 compositional variations is indicated, whereby a greater sheet-silicate content results in  
660 an increase in the thickness of the deformation-induced structures, the density of the  
661 structures and the volume percentage that both localized and distributed deformation  
662 occupies (Fig. 6b,c and Table1). This correlation is less obvious for the aplitic boundary  
663 facies as well as the Southwestern Aar granite. There is a large amount of pervasive  
664 deformation within these relatively poor sheet-silicate-content rocks. This discrepancy  
665 may arise from boundary effects due to the limited length of the transect studies (several  
666 hundred meters; Fig. 6a). A relatively large part of the transect length is occupied by  
667 intensely deformed lithological contacts. Furthermore, both the aplitic boundary facies  
668 and the Southwestern Aar granite are located close to the very highly strained Grimsel  
669 Zone that may shield them from more intense deformation by being more efficient as it is  
670 weaker for deformation.

671       Generally these observations illustrate that, although on the meter scale,  
672 localization occurs, on the scale of several km, deformation may be described by  
673 homogeneous strain distribution over a multitude of shear zones. Smaller structures  
674 dominate in the sheet-silicate-poor areas, compared to meter-scale shear zones in the  
675 sheet-silicate-rich zones. At least in the case of our mid-crustal section, deformation is  
676 never localized along only one major shear zone, but is always distributed.

#### 677 5.4 Geodynamic implications

678 Based on deformation overprinting relations in the Mesozoic sediments of the  
679 autochthonous cover of the Aar massif and the Helvetic nappes, a kinematic model for  
680 their evolution has already been postulated (Burkhard 1988; Herwegh and Pfiffner 2005).  
681 Based on our new results, we can refine this sequence because our data and conceptual  
682 framework for the shear zone pattern, and its kinematics and evolution through time, both  
683 provide new information for Alpine deformation on a regional scale and have important  
684 geodynamic implications.

685 Kinematic analysis of the Handegg phase and its associated orientations of the  
686 structures give first hints for a NW-SE related shortening associated with strong reverse  
687 faulting (Fig. , 13a,c). The activity of the associated shear zones has been dated at 22-17  
688 Ma (Challandes et al., 2008; Rolland et al., 2009). This time interval correlates with the  
689 two deformation stages described by Burkhard (1988). The first stage, (Kiental phase of  
690 Burkhard, 1988), is defined by NW-directed thrusting and large-scale recumbent folding  
691 in the Doldenhorn nappe at around 30-20 Ma. In the subsequent Grindelwald phase, both  
692 the entire Helvetic nappe stack and the basement rocks of the Aar massif are updomed at  
693 20 to 5 Ma (Burkhard, 1988).

694 The present day steep orientation (Fig. 2b) of the Handegg phase shear zones is  
695 unfavorably oriented for thrusting, however, their present day orientation may not match  
696 their orientation during shear, but even allowing for that possibility, they were likely  
697 steeply dipping requires other conditions to be active structures. Such high-formation  
698 angles may result from low differential stresses and/or high pore-fluid pressures (e.g.,

699 Sibson et al., 1988). The evolution of the Handegg structures might therefore be  
700 attributed to later stage shortening of the Kiental phase.

701 Ongoing NW-SE compression of the over-thickened crust and the steepening of  
702 Handegg phase shear planes resulted in lateral orogen-parallel extension, accommodated  
703 first by a gradual transition from Handegg to Oberaar phase oblique shearing component  
704 (strong vertical component), and then by Oberaar strike-slip shearing under greenschist  
705 facies metamorphic conditions ( $> 400^{\circ}\text{C}$ ). Therefore, a transpressional kinematic regime  
706 locally evolved during the Oberaar deformation phase.

707 At the larger scale, orogen-parallel dextral movement occurred simultaneously with  
708 the Oberaar phase along the Rhône Valley (Campani et al., 2010) and the Chamonix  
709 valley between the external Aiguilles Rouges massif and more internal Mont Blanc  
710 massif (Egli and Mancktelow, 2013). These structures are in part linked with the  
711 Simplon-fault system (Hubbard and Mancktelow, 1992). Consequently, en-echelon  
712 arranged strike-slip lateral ramps at the northern extent of the Rhone-Simplon Line can be  
713 correlated with the Oberaar phase of dextral shearing, which has been previously implied  
714 by other studies (Rolland et al., 2009).

## 715 **6 Conclusions**

716 Alpine age mid-crustal deformation reported in this study was strongly controlled  
717 by a combination of reactivation of pre-existing mechanical anisotropies and variations in  
718 the effective viscosity of the host rocks. Pre-Alpine anisotropies included a pre-Alpine  
719 foliation in the (pre-) Variscan basement in the Grimsel Zone, compositional variations in  
720 sheet-silicate content of magmatic host rocks as well as their lithological contacts. These

721 pre-existing heterogeneities were used during both the Alpine Handegg and Oberaar  
722 deformation phases, where strain partitioned between volumetrically important  
723 background strain and deformationally important, highly localized strain in shear zones.  
724 Interestingly, the quartz-rich rocks, i.e. felsic magmatic host-rocks (CAGr, SWAGr,  
725 aplites), represent the mechanically more rigid bodies in this mid-crustal section,  
726 although conditions of ductile deformation of quartz were reached. Instead, bulk  
727 deformation was focussed in the more mafic rocks (GrGr, metabasic dikes) due to their  
728 abundant sheet-silicate contents. Consequently, the spatial distribution of these mafic  
729 rocks controlled to some extent the concentration of shear zones in these mafic domains  
730 (Fig. 12b). In terms of localized deformation in wide ( $> 1$  m shear zone thickness) high  
731 strain zones, they occur commonly along lithological/compositional contacts, probably  
732 owing to stress concentrations. Nonetheless the multitude of thin ( $< 0.2$  m wide) but  
733 several 100-m-to-kilometers-long shear zones, dissecting the entire width of pre-existing  
734 granitoids, created a very well developed strain localization pattern. In the homogeneous  
735 plutonic host rocks (CAGr, SWAGr), several lines of evidence point toward shear-zone  
736 nucleation along brittle fractures followed by ductile deformation during shearing (Figs.  
737 5, 12c). Here, strain weakening due to mechanical grain-size reduction and reactions via  
738 chemical mass-transfer processes result in sheet-silicate-enriched, fine-grained  
739 polymineralic ultramylonites, facilitating ductile deformation along the high-strain zones  
740 (Stünitz and Fitzgerald, 1993; Füsseis and Handy, 2008). In this way, two different  
741 deformation histories, one brittlely-based and the other ductiley-based, led to the same  
742 outcome of deformation localized in shear zones as a function of the initial material  
743 properties of the host.

744 Kinematically, a change from a contractional to a local transpressional setting is  
745 observed where:

746 The Handegg phase is marked by shortening in combination with dominant south-block-  
747 up shearing under greenschist facies conditions, resulting in crustal thickening.

748 Shear zones range from mm- to m-scale, and are the dominant type of shear zone  
749 throughout the area.

750 The Oberaar phase is characterized by transpression and dextral strike-slip deformation,  
751 still under greenschist facies conditions. In the Grimsel Zone, these shear zones  
752 form a large dextral domain, whereas in the post-Variscan intrusives they are  
753 narrower and more discrete. Retrograde deformation affected some of the Oberaar  
754 phase shear zones.

755 In conclusion, the classical “anastomosing” deformation pattern of the Grimsel  
756 shear zones is not the result of a single deformation event. Rather the deformation pattern  
757 progressively evolved during a complex and long-lived deformation history that  
758 combined a changing kinematic framework, with variable sheet-silicate contents in  
759 different units controlling shear-zone initiation along a variety of pre-Alpine geometrical  
760 anisotropies. In this sense, initial mid-crustal heterogeneity has a major effect on the  
761 control of mid-crustal deformation in the Aar massif up to the present day.

762

### 763 **Acknowledgements**

764 We would like to thank the following people and institutions for their support in  
765 our project: KWO, NAGRA, Raphael Schneeberger, Samuel Mock, Guido Schreurs, Max  
766 Peters, Armin Dielfolder, Tom Belgrano and Daniel Egli. The article greatly benefitted

767 from the thorough reviews of D. Czeck and R. Law as well as the excellent editorial  
768 handling by W. Dunne. Financial support by SNF (project 200021 132196) is greatly  
769 acknowledged.

770

771

772 **References:**

773 Abrecht, J., 1994. Geologic units of the Aar massif and their pre-Alpine rock  
774 associations: a critical review: The pre-Alpine crustal evolution of the Aar-, Gotthard-and  
775 Tavetsch massifs. Schweizerische mineralogische und petrographische Mitteilungen 74,  
776 5-27.

777

778 Alsop, G.I., Holdsworth, R.E., 2002. The geometry and kinematics of flow perturbation  
779 folds. Tectonophysics 350, 99-125.

780

781 Bambauer, H., Herwegh, M., Kroll, H., 2009. Quartz as indicator mineral in the Central  
782 Swiss Alps: the quartz recrystallization isograd in the rock series of the northern Aar  
783 massif. Swiss Journal of Geosciences 102, 345-351.

784

785 Bambauer, H.U., Bernotat, W., Breit, U., Kroll, H., 2005. Perthitic alkali feldspar as  
786 indicator mineral in the Central Swiss Alps. Dip and extension of the surface of the  
787 microcline/sanidine transition isograd. European Journal of Mineralogy 17, 69-80.

788

789 Baumberger, R., Herwegh, M., Kissling, E. (in review). Lineament and Shear zone map  
790 of the Central Aar massif: An approach for consistent mapping in large and high-relief  
791 regions. Swiss Journal of Geosciences.

792

793 Belgrano, T., Herwegh, M., Berger, A., 2016. Inherited structural controls on fault  
794 geometry, architecture and hydrothermal activity: An example from Grimsel Pass,  
795 Switzerland. Swiss Journal of Geosciences, doi 10.1007/s00015-016-0212-9.

796

797 Bell, T.H., 1978. Progressive deformation and reorientation of fold axes in a ductile  
798 mylonite zone: the Woodroffe thrust. Tectonophysics, 44, 285-298.

799

800 Bousquet, R., 2012. Metamorphic framework of the Alps. CCGM/CCMW.

801

802 Burkhard, M., 1988. L'Helvétique de la bordure occidentale du massif de l'Aar (évolution  
803 tectonique et métamorphique). Eclogae Geologicae Helvetiae 81, 63-114.

804

805 Campani, M., Mancktelow, N., Seward, D., Rolland, Y., Müller, W., Guerra, I., 2010.

806 Geochronological evidence for continuous exhumation through the ductile - brittle

807 transition along a crustal - scale low - angle normal fault: Simplon Fault Zone, central

808 Alps. Tectonics 29.

809

810 Carreras, J., Czeck, D.M., Druguet, E., Hudleston, P.J., 2010. Structure and development  
811 of an anastomosing network of ductile shear zones. *Journal of Structural Geology* 32,  
812 656-666.

813

814 Challandes, N., Marquer, D., Villa, I., 2008. P-T-t modelling, fluid circulation, and <sup>39</sup>Ar-  
815 <sup>40</sup>Ar and Rb-Sr mica ages in the Aar Massif shear zones (Swiss Alps). *Swiss Journal of*  
816 *Geosciences* 101, 269-288.

817

818 Choukroune, P., Gapais, D., 1983. Strain pattern in the Aar Granite (Central Alps):  
819 Orthogneiss developed by bulk inhomogeneous flattening. *Journal of Structural Geology*  
820 5, 411-418.

821

822 Dollinger, H., 1989. Petrographische und geochemische Untersuchungen des  
823 Altkristallins zwischen Nägelisgrätli und Oberaarjoch:(Grimsel, Kt. Bern);  
824 Hydrothermale Veränderung granitischer Gesteine in der Grimselregion:(Mittleres  
825 Aarmassiv), PhD Thesis, University of Bern.

826

827 Ebert, A., Herwegh, M., Pfiffner, A., 2007. Cooling induced strain localization in  
828 carbonate mylonites within a large-scale shear zone (Glarus thrust, Switzerland). *Journal*  
829 *of Structural Geology* 29, 1164-1184.

830

831 Egli, D., Mancktelow, N., 2013. The structural history of the Mont Blanc massif with  
832 regard to models for its recent exhumation. *Swiss Journal of Geosciences* 106, 469-489.

833

834 Fousseis, F., Handy, M.R., Schrank, C., 2006. Networking of shear zones at the brittle-to-  
835 viscous transition (Cap de Creus, NE Spain). *Journal of Structural Geology* 28, 1228-  
836 1243.

837

838 Gapais, D., Bale, P., Choukroune, P., Cobbold, P., Mahjoub, Y., Marquer, D., 1987. Bulk  
839 kinematics from shear zone patterns: some field examples. *Journal of Structural Geology*  
840 9, 635-646.

841

842 Goncalves, P., Oliot, E., Marquer, D., Connolly, J.A.D., 2012. Role of chemical  
843 processes on shear zone formation: an example from the Grimsel metagranodiorite (Aar  
844 massif, Central Alps). *Journal of Metamorphic Geology* 30, 703-722.

845

846 Guermani, A., Pennacchioni, G., 1998. Brittle precursors of plastic deformation in a  
847 granite: an example from the Mont Blanc massif (Helvetic, western Alps). *Journal of*  
848 *Structural Geology* 20, 135-148.

849

850 Handy, M.R., Hirth, G., Bürgmann, R., 2007. Continental fault structure and rheology  
851 from the frictional-to-viscous transition downward, in: Handy, M.R., Hirth, G., Hovius,  
852 N. (Eds.), *Tectonic Faults Agents of Change on a Dynamic Earth*. MIT Press.

853

854 Haertel, M., Herwegh, M. 2014. Microfabric memory of vein quartz for strain  
855 localization in detachment faults: A case study on the Simplon fault zone. *Journal of*  
856 *Structural Geology* 68, 16-32, doi.org/10.1016/j.jsg.2014.08.001.  
857

858 Herwegh, M., Berger, A., Ebert, A., Brodhag, S., 2008. Discrimination of annealed and  
859 dynamic fabrics: Consequences for strain localization and deformation episodes of large-  
860 scale shear zones. *Earth and Planetary Science Letters* 276, 52-61.  
861

862 Herwegh, M., Linckens, J., Ebert, A., Berger, A., Brodhag, S.H., 2011. The role of  
863 second phases for controlling microstructural evolution in polymineralic rocks: A review.  
864 *Journal of Structural Geology* 33, 1728-1750.  
865

866 Herwegh, M., Mercolli, I., Linckens, J., Muentener, O., 2016. Mechanical anisotropy  
867 control on strain localization in upper mantle shear zones. *Tectonics* 35, 1177-1204,  
868 doi:10.1002/2015TC004007  
869

870 Herwegh, M., Pfiffner, O.A., 2005. Tectono-metamorphic evolution of a nappe stack: A  
871 case study of the Swiss Alps. *Tectonophysics* 404, 55-76.  
872

873 Horsman, E., Tikoff, B., Czeck, D., 2008. Rheological implications of heterogeneous  
874 deformation at multiple scales in the Late Cretaceous Sierra Nevada, California. *GSA*  
875 *Bulletin*, 120, 238-255, doi: 10.1130/B26161.1.  
876

877 Hubbard, M., Mancktelow, N.S., 1992. Lateral displacement during Neogene  
878 convergence in the western and central Alps. *Geology* 20, 943-946.  
879

880 Keusen, H.R., Ganguin, J., Schuler, P., Buletti, M., 1989. Grimsel test site – *Geology*,  
881 Nagra technical report NTB 87-14E, Nagra, Wetingen, Switzerland, Nagra technical  
882 report. NAGRA.  
883

884 Labhart, T.P., 1977. Aarmassiv und Gotthardmassiv. Gebruder Borntraeger  
885 Verlagsbuchhandlung.  
886

887 Mancktelow, N.S., 2002. Finite-element modelling of shear zone development in  
888 viscoelastic materials and its implications for localisation of partial melting. *Journal of*  
889 *Structural Geology* 24, 1045-1053.  
890

891 Mancktelow, N.S., Pennacchioni, G., 2005. The control of precursor brittle fracture and  
892 fluid-rock interaction on the development of single and paired ductile shear zones.  
893 *Journal of Structural Geology* 27, 645-661.  
894

895 Marquer, D., Challandes, N., Baudin, T., 1996. Shear zone patterns and strain distribution  
896 at the scale of a Penninic nappe: the Suretta nappe (Eastern Swiss Alps). *Journal of*  
897 *Structural Geology* 18, 753-764.  
898

899 Marquer, D., Gapais, D., Capdevila, R., 1985. Comportement chimique et  
900 orthogneissification d'une granodiorite en facies schistes verts (Massif de l'Aar, Alpes  
901 Centrales). Bulletin de minéralogie 108, 209-221.  
902

903 Means, W.D., 1995. Shear zones and rock history. Tectonophysics 247, 157-160.  
904

905 Menegon, L., Pennacchioni, G., 2010. Local shear zone pattern and bulk deformation in  
906 the Gran Paradiso metagranite (NW Italian Alps). International Journal of Earth Sciences  
907 99, 1805-1825.  
908

909 Niggli, C.R., 1965. Petrographie und Petrogenesis der Migmatite und Gneise im  
910 südlichen Aarmassiv zwischen Obergesteln und Furkapass, PhD Thesis, University of  
911 Bern.  
912

913 Oberhänsli, R., 1986. Geochemistry of meta-lamprophyres from the Central Swiss Alps.  
914 Schweizerische mineralogische und petrographische Mitteilungen 66.  
915

916 Oliot, E., Goncalves, P., Marquer, D., 2010. Role of plagioclase and reaction softening in  
917 a metagranite shear zone at mid-crustal conditions (Gotthard Massif, Swiss Central Alps).  
918 Journal of Metamorphic Geology 28, 849-871.  
919

920 Ortner, H., Reiter, F., Acs, P., 2002. Easy handling of tectonic data: the programs  
921 TectonicVB for Mac and TectonicsFP for Windows™. *Computers & Geosciences* 28,  
922 1193-1200.  
923

924 Paterson, M.S., 1995. A theory for granular flow accommodated by material transfer via  
925 an intergranular fluid. *Tectonophysics* 245, 135-151.  
926

927 Pennacchioni, G., 2005. Control of the geometry of precursor brittle structures on the  
928 type of ductile shear zone in the Adamello tonalites, Southern Alps (Italy). *Journal of*  
929 *Structural Geology* 27, 627-644.  
930

931 Pennacchioni, G., Mancktelow, N.S., 2007. Nucleation and initial growth of a shear zone  
932 network within compositionally and structurally heterogeneous granitoids under  
933 amphibolite facies conditions. *Journal of Structural Geology* 29, 1757-1780.  
934

935 Peters, M., Veveakis, M., Poulet, T., Karrech, A., Herwegh, M., Regenauer-Lieb, K.  
936 2015. Boudinage as a material instability of elasto-visco-plastic rocks. *Journal of*  
937 *Structural Geology* 78, 86-102.

938 Platt, J.P., Behr, W.M., 2011. Grainsize evolution in ductile shear zones: Implications for  
939 strain localization and the strength of the lithosphere. *Journal of Structural Geology* 33,  
940 537-550.  
941

942 Ramsay, J.G., 1980. Shear zone geometry: a review. *Journal of Structural Geology* 2, 83-  
943 99.  
944

945 Raynaud, S., Vasseur, G., 2014. Shear failure mechanism in granite inferred from multi-  
946 scale brittle structures. *Journal of Structural Geology* 66, 42-57.  
947

948 Rolland, Y., Cox, S.F., Corsini, M., 2009. Constraining deformation stages in brittle-  
949 ductile shear zones from combined field mapping and  $^{40}\text{Ar}/^{39}\text{Ar}$  dating: The structural  
950 evolution of the Grimsel Pass area (Aar Massif, Swiss Alps). *Journal of Structural*  
951 *Geology* 31, 1377-1394.  
952

953 Rolland, Y., Rossi, M., Cox, S., Corsini, M., Mancktelow, N., Pennacchioni, G., Fornari,  
954 M., Boullier, A., 2008.  $^{40}\text{Ar}/^{39}\text{Ar}$  dating of synkinematic white mica: insights from  
955 fluid-rock reaction in low-grade shear zones (Mont Blanc Massif) and constraints on  
956 timing of deformation in the NW external Alps. *Geological Society, London, Special*  
957 *Publications* 299, 293-315.  
958

959 Rossi, M., Rolland, Y., Vidal O., Cox, S.F. 2005. Geochemical and element transfer  
960 during shear-zone development and related episyenites at middle crust depths: insights  
961 from the Mont Blanc granite (French - Italian Alps). *Geol. Soc. Spec. Publ.* 245, 373-396.  
962

963 Schaltegger, U., 1989. Geochemische und isotopengeochemische Untersuchungen am  
964 zentralen Aaregranit und seinen assoziierten Gesteinen zwischen Aare und Reuss  
965 (Aarmassiv, Schweiz), PhD Thesis, University of Bern.

966

967 Schaltegger, U., 1990. Post-magmatic resetting of Rb-Sr whole rock ages — a study in  
968 the Central Aar Granite (Central Alps, Switzerland). *Geologische Rundschau* 79, 709-  
969 724.

970

971 Schaltegger, U., 1993. The evolution of the polymetamorphic basement in the Central  
972 Alps unravelled by precise U-Pb zircon dating. *Contributions to Mineralogy and*  
973 *Petrology* 113, 466-478.

974

975 Schaltegger, U., 1994. Unravelling the pre-Mesozoic history of Aar and Gotthard massifs  
976 (Central Alps) by isotopic dating: a review : The pre-Alpine crustal evolution of the Aar-,  
977 Gotthard- and Tavetsch massifs. *Schweizerische mineralogische und petrographische*  
978 *Mitteilungen* 74, 41-51.

979

980 Schaltegger, U., Abrecht, J., Corfu, F., 2003. The Ordovician orogeny in the Alpine  
981 basement: constraints from geochronology and geochemistry in the Aar Massif (Central  
982 Alps). *Swiss Bulletin of Mineralogy and Petrology* 83, 183-239.

983

984 Schaltegger, U., Corfu, F., 1992. The age and source of late Hercynian magmatism in the  
985 central Alps: evidence from precise U–Pb ages and initial Hf isotopes. *Contributions to*  
986 *Mineralogy and Petrology* 111, 329-344.  
987

988 Schneider, T.R., 1974. Grimselstollen, Transitgas AG pipeline, Niederlande- Italien  
989 Abschnitt Schweiz. Elektro-Watt Ingenieurunternehmung AG Zurich.  
990

991 Segall, P., Simpson, C. 1986. Nucleation of ductile shear zones on dilatant fractures.  
992 *Geology*, 14, 56-59.  
993

994 Shimamoto, T., 1989. The origin of S-C mylonites and a new fault-zone model. *Journal*  
995 *of Structural Geology* 11, 51-64.  
996

997 Sibson, R.H., Robert, F., Poulsen, K.H. 1988. High-angle reverse faults, fluid-pressure  
998 cycling, and mesothermal gold-quartz deposits. *Geology* 16, 551-555.  
999

1000 Stalder, H.A., 1964. Petrographische und mineralogische Untersuchungen im  
1001 Grimselgebiet (mittleres Aarmassiv), PhD Thesis, University of Bern.  
1002

1003 Steck, A., 1968. Die alpidischen Strukturen in den Zentralen Aaregraniten des westlichen  
1004 Aarmassivs. *Eclogae Geologicae Helvetiae* 61, 19-48.  
1005

1006 Stünitz, H., Fitz Gerald, J., 1993. Deformation of granitoids at low metamorphic grade.  
1007 II: Granular flow in albite-rich mylonites. *Tectonophysics* 221, 299-324.  
1008

1009 Vernon, R.H., and Flood, R.H., 1988, Contrasting deformation of S- and I-type granitoids  
1010 in the Lachlan fold belt, eastern Australia: *Tectonophysics*, v. 147, p. 127–143, doi:  
1011 10.1016/0040-1951(88)90152-7.  
1012

1013 Wehrens, P. (2015): Structural evolution in the Aar Massif (Haslital transect):  
1014 Implications for mid-crustal deformation. PhD thesis University Bern  
1015

1016 Wehrens, P., Berger, A., Herwegh, M., Peters, M., Spillmann, T. (in press): Deformation  
1017 at the frictional-viscous transition: Evidence for cycles of fluid-assisted embrittlement  
1018 and ductile deformation in the granitoid crust. In press at *Tectonophysics*.  
1019

1020 Wintsch, R.P., Aleinikoff, J.N., Keewook, Y., 2005. Foliation development and reaction  
1021 softening by dissolution and precipitation in the transformation of granodiorite to  
1022 orthogneiss, Glastonbury Complex, Connecticut, U.S.A. *The Canadian Mineralogist*, 43,  
1023 327-347.  
1024

1025 Ziegler, M., Loew, S., Moore, J.R., 2013. Distribution and inferred age of exfoliation  
1026 joints in the Aar Granite of the central Swiss Alps and relationship to Quaternary  
1027 landscape evolution. *Geomorphology* 201, 344-362.  
1028

1029 **Figure captions**

1030 Fig. 1: Overview map of the Aar massif with the Haslital transect from Meiringen  
1031 to Grimsel Pass (modified from Goncalves et al., 2012). Main map is an  
1032 inset of the map of Switzerland on the upper left and small inset in the map  
1033 shows study area (Fig. 2). Swiss coordinates are given in km.

1034 Fig. 2: (a) Geological map of the Haslital area [based on Stalder (1964), Steck  
1035 (1968), Abrecht (1994) and our own observations] containing a pervasive  
1036 pattern of ductile shear zones. Major and minor shear zones are represented  
1037 by thick and thin lines, respectively. (b) Lower-hemisphere equal-area  
1038 projections of both poles to the shear planes and the stretching lineations for  
1039 the five analysed units investigated in this study. Shear senses are color-  
1040 coded by the symbols.

1041 Fig. 3: Weakly deformed host rock (left column) with corresponding strongly  
1042 deformed tectonite (central column). Right column indicates both sheet  
1043 silicate content (light grey) and strain intensity variation in background  
1044 (blue gradient) and high strain zones (red gradient). Note, the greater the  
1045 sheet silicate content the greater the strain intensity as manifested by an  
1046 increase in foliation intensity and grain-size reduction. CAGr: Central Aar  
1047 granite; GrGr: Grimsel granodiorite; SWAGr: Southwestern Aar granite.  
1048 Grimsel Zone belongs to pre-Variscan basement, where  $S_{\text{prealp}}$  shows a  
1049 folded pre-Alpine foliation. Magmatic dikes are situated in CAGr. Table 1  
1050 contains data about detailed mineral contents.

1051 Fig. 4: Strain gradients in the granodiorite. Foliation intensity varies from weak  
1052 (left) to moderate (right) owing to the increased biotite content of the  
1053 granodiorite. (b) Mylonitic granodiorite. (c) Transition from mylonitic  
1054 (right) to ultramylonitic (left) granodiorite.

1055 Fig. 5: Evidence for brittle deformation in the granitoid rocks. (a-c) Ultramylonitic  
1056 shear zone in weakly deformed Central Aar Granite (CAGr). (a) Overview  
1057 image showing an ultramylonitic shear zone adjacent to networks of sub-  
1058 parallel biotite(bt)-coated fractures. (b) Enlarged view documents that the  
1059 fracture network is cut and overprinted by the ultramylonite. (c) The  
1060 ultramylonite widens at its end into a horse tail structure consisting of brittle  
1061 biotite-coated fractures. (d) Mylonitic shear zone in a strongly foliated  
1062 Grimsel granodiorite (GrGr) cut by a retrograde brittle cataclastic zone. (e)  
1063 Weakly foliated GrGr from the nagra (National Cooperative for the  
1064 Disposal of Radioactive Waste) Grimsel Test Side overprinted by a  
1065 hydrothermally altered cataclasite. Size of pen used for scale approx. 15 cm.

1066 Fig. 6: Data gathered from the Transitgas tunnel (Schneider, 1974) to quantify  
1067 strain distribution. a) Frequency histogram of the abundance of all mylonitic  
1068 and cataclastic zones as a function of position along the tunnel transect.  
1069 Profile positions of lithological units are indicated. b) Summary of number  
1070 of deformation structures per km according to their thicknesses for each  
1071 lithological unit. Red shading connects large-scale shear zones with  
1072 thicknesses  $>0.5$  m c) Percentage of rock volume for each unit affected by  
1073 a specific deformation structure. CAGr: Central Aar granite; GrGr: Grimsel

1074 granodiorite; ABF: aplitic boundary facies, GSZ: Grimsel Zone, SWAGr:  
1075 Southwestern Aar granite.

1076 Fig. 7: Shear zone maps of the study area between Rättrichsbodensee (R) and  
1077 Gletsch. a) Handegg phase shear zones. Note the increase in density and  
1078 thickness of the shear zones from the Central Aar granite to Grimsel  
1079 granodiorite. White arrows indicate Handegg phase shear zones cut by the  
1080 large-scale Grimsel Pass Shear zone (GPSZ). (b) Oberaar phase (a), (b) and  
1081 (c) shear zones. Note the set of thick dextral shear-zones at Oberaarsee (see  
1082 Figure 2a for locations) presenting the GPSZ. Radiometric ages are from  
1083 Challandes et al. (2008, with asterisk) and Rolland et al. (2009). Capital  
1084 letters B-F show locations of supplementary Figures B-F also documenting  
1085 cross-cutting relationships.

1086 Fig. 8: Lower-hemisphere equal-area plots showing the orientations of the shear  
1087 planes (great circles) and related stretching lineations for the Handegg phase  
1088 (left column) and Oberaar phase (right column) structures in the different  
1089 lithological units (CAGr: Central Aar granite, GrGr: Grimsel granodiorite,  
1090 GSZ: Grimsel Zone, SWAGR: Southwestern Aar granite, AAZ: Ausserberg  
1091 –Avat Zone.). Handegg phase: empty squares and filled red circles indicate  
1092 stretching lineations of normal (stippled great circles) and reverse (solid  
1093 great circles) shear zones. Red domain represents manually drawn envelope  
1094 of the majority of the shear planes. Oberaar phase: filled blue (dextral)  
1095 circles and empty blue (sinistral) squares show stretching lineations of  
1096 Oberaar<sub>a</sub> shear zone orientations; filled blue (dextral) rhombs and empty

1097 blue (sinistral) rhombs show stretching lineations of Oberaar<sub>b</sub> shear zone  
1098 orientations; black filled circles (dextral) and empty squares (sinistral)  
1099 represent stretching lineations of Oberaar<sub>c</sub> shear zone orientations. Dark and  
1100 bright blue shading present manually drawn envelopes of the majority of the  
1101 dextral (solid great circles; Oberaar<sub>a</sub> and Oberaar<sub>b</sub> orientations) and sinistral  
1102 (Oberaar<sub>c</sub> orientations) (stippled great circles) shear planes, respectively.

1103  
1104 Fig. 9: Field examples showing crosscutting of older Handegg structures by  
1105 younger Oberaar shear zones (left column: field photographs, right column:  
1106 schematic drawings). All images are in map view. Shear senses and  
1107 orientation of lineations are indicated. (a,b) Southwestern Central Aar  
1108 granite (SCAGr) outcrop with an old Handegg phase related foliation (S<sub>H</sub>)  
1109 which is cut (i) by a dextral shear zone in Oberaar<sub>a</sub> orientation (SZ<sub>Oa</sub>), (ii) A  
1110 sinistral shear zone in Oberaar<sub>c</sub> orientation (SZ<sub>Oc</sub>) and (iii) shear bands in  
1111 Oberaar<sub>b</sub> orientations (S<sub>Ob</sub>). (c,d) Grimsel granodiorite outcrop showing a  
1112 dextral Oberaar<sub>a</sub> phase shear zone (SZ<sub>Oa</sub>) with S-C fabric being cut by a  
1113 dextral Oberaar<sub>b</sub> phase (SZ<sub>Ob</sub>) shear zone. Note the moderately SE dipping  
1114 lineations indicating dextral oblique slip. (e,f) Grimsel granodiorite (GrGr)  
1115 outcrop where an Oberaar<sub>b</sub> phase shear zone (SZ<sub>Ob</sub>) runs along an aplitic  
1116 body and crosscuts a Handegg phase shear zone (SZ<sub>H</sub>). Note the steeply  
1117 South plunging and subhorizontal SE plunging stretching lineations of the  
1118 Handegg- and Oberaar-phase shear zones.

1119 Fig. 10: Detailed map of the shear zone at the west end of Oberaarsee (see Figure  
1120 2a for location names). An old Handegg-Phase foliation in the  
1121 Grimselgranodiorite (GrGr) is cut by a branch of the the large-scale Grimsel  
1122 Pass shear zone (GSPZ). Lineations and shear sense indicators (e.g. C'  
1123 structures, asymmetrically folded veins) document Oberaar Phase dextral  
1124 strike slip to oblique slip.

1125 Fig. 11: Field images (left column) and micrographs (right column) of magmatic  
1126 Central Aar granite (CAGr) fabrics (a,b) as well as of Handegg- and  
1127 Oberaar-phase shear zones (c-h). Appearance of isotropic CAGr at (a) the  
1128 outcrop and (b) in thin section (from nagra Grimsel Test Site) with quartz  
1129 (qtz), biotite (bt), chlorite (Chl) and k-feldspar (k-fsp). (c) Detail of  
1130 mylonitic Handegg-phase shear zone (667231/162323) in Central Aar  
1131 granite (subvertical section) showing in (d) an electron backscatter image of  
1132 a polymineralic matrix (mainly biotite, quartz, feldspar) and dynamically  
1133 recrystallized quartz bands. Note the smaller quartz and albite grain size  
1134 (dashed box), being pinned by finely dispersed biotite in the polymineralic  
1135 matrix, compared to the grain sizes in the monomineralic quartz band (qtz).  
1136 (e) Oberaar<sub>a</sub>-phase shear zone in Grimsel Zone (668010/157059) with a C'  
1137 structure indicating a dextral shear sense. (f) Thin-section showing a high  
1138 temperature stage (Oberaar phase), where both white mica (wm) and biotite  
1139 show stable coexistence in the same polymineralic microstructure during  
1140 grain refinement by recrystallization (compare grain sizes with magmatic  
1141 fabrics in b). (g) S-C fabric in SouthwesternAar granite (669630/157118)

1142 indicating a dextral shear sense, where the C plane represents an Oberaar<sub>b</sub>  
1143 phase shear zone. (h) Thin-section of an Oberaar<sub>b</sub> phase shear zone in  
1144 SWAGr, recrystallized interconnected white mica bands parallel to C plane  
1145 (entire section) dominate the ultramylonitic fabric demonstrating the lower  
1146 temperature conditions. Diameters of pens are about 7-8 millimeters.

1147 Fig. 12 A schematic overview of shear zone initiation and evolution. (a) Vertical N–  
1148 S cross section representing pre-Alpine anisotropies and their differences in  
1149 sheet-silicate content are illustrated from north to south, as well as a  
1150 predefined fabric for the Grimsel Zone (GSZ). (b) The initial sheet-silicate  
1151 content is a control of deformation distribution during the Handegg phase:  
1152 (i) enhanced sheet-silicate contents result in wide ductile shear zones, (ii)  
1153 brittle fractures present the precursors of subsequent ductile deformation in  
1154 granitoids with low sheet-silicate content. c) With ongoing shearing initially  
1155 brittle fractures are affected by a shear zone widening (iii) and broader  
1156 ductile shear zones also develop here. Some of the shear zones are affected  
1157 by a retrograde overprint and associated localization, first during late  
1158 Handegg phase then during the Oberaar phase, forming first white mica  
1159 domains and then cataclasites and fault gouges (iv).

1160 Fig. 13: a, c) Lower-hemisphere equal-area plots and block diagram of Handegg  
1161 phase shear zones, b,d) same presentation but for Oberaar phase shear  
1162 zones. The large Oberaar phase dextral domain in the south of the study  
1163 area is indicated as an analogue to the Grimsel Zone. Handegg phase shear  
1164 zones are cross-cut by Oberaar phase zones (a) and (b). Within the large

1165 Oberaar<sub>a</sub> phase strain domains, C' structures developed with progressive  
1166 dextral strike-slip/oblique-slip shearing. Within the more homogenous rocks  
1167 to the north, a conjugate set with dominant synthetic and some antithetic  
1168 Riedel shears developed (Oberaar<sub>b</sub> and Oberaar<sub>c</sub> phase). The block diagram  
1169 shows the complex pattern of lensoid-shaped, weakly deformed domains  
1170 separated by high strain shear zones. Note that the block diagrams of (b,d)  
1171 are slightly rotated with respect to north for illustration purposes.

1172

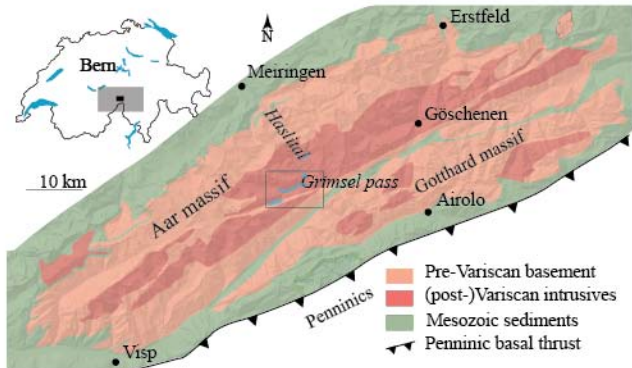
1173 Table 1, Composition of the lithological units. The most important minerals in  
1174 vol% are stated, as well as the data source. Note the distinct variation in  
1175 sheet silicate content. Data sources are: Stalder, 1964; Niggli, 1965; Keusen  
1176 et al., 1987; Schaltegger 1989. In Bt column green colour reflects high  
1177 biotite content. Red colour reflects low biotite content. Qtz = quartz, Kfs =  
1178 potassium feldspar, PL = plagioclase, Bt = biotite, Wm = white mica, Chl=  
1179 chlorite, Ep = epidote.

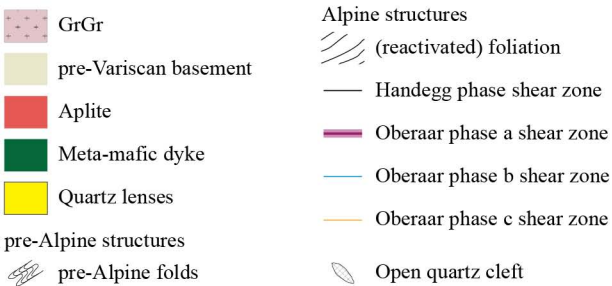
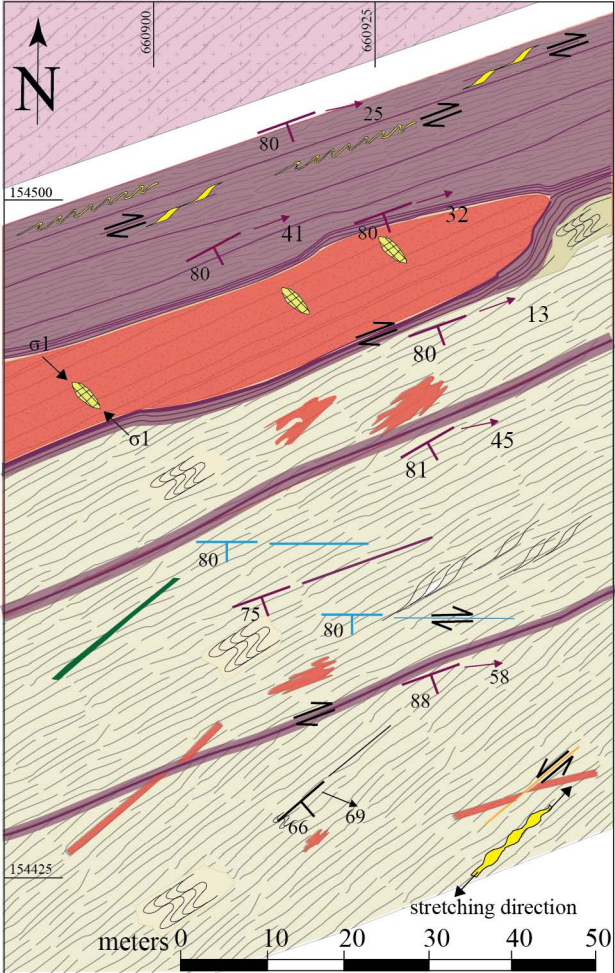
1180 Table 2, Correlation of deformation phases from this study to previous work. Note  
1181 that Stage 1 (Rolland et al., 2009) has a much larger variation in shear plane  
1182 orientation than the Handegg phase and Stage 3 is sinistral although  
1183 Oberaar<sub>b</sub> phase is dextral.

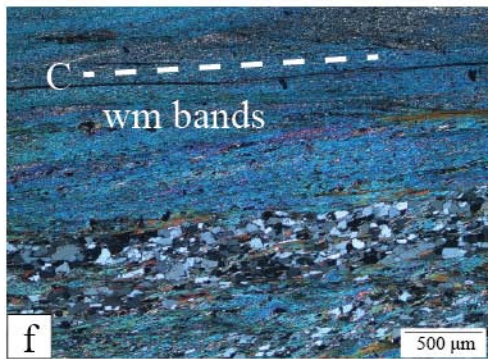
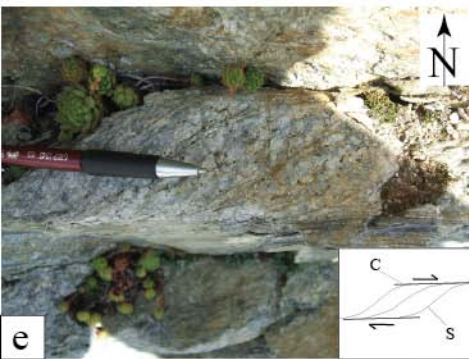
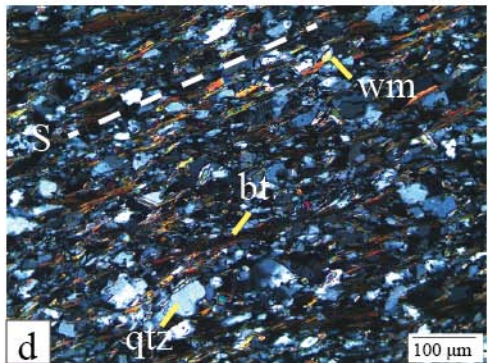
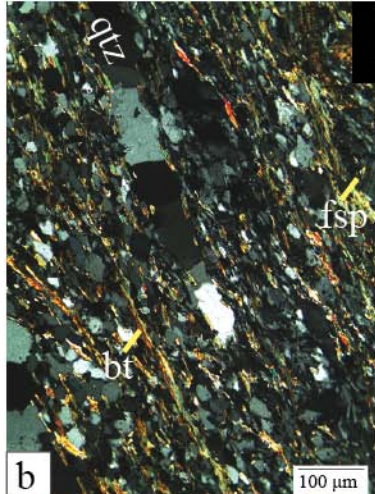
1184 Table 3, Description and characteristics of shear zones with large thickness. Shear  
1185 zone locations shown in Fig. 7.

1186 Table 4, Summary of microstructures in samples analyzed (X and Y are Swiss  
1187 coordinates. Deformation features observed in thin section include:  
1188 dominant quartz recrystallization (REX) mechanism within monomineralic  
1189 quartz aggregates (BLG - bulging, SGR - subgrain rotation). Compositional  
1190 information is the dominant mica, the associated mica with quartz  
1191 recrystallization, which mica occupies the strain shadows, minerals building  
1192 continuous bands. Assignation to deformation phase in most rightward  
1193 column. Note, although all phases have similar mineral stabilities, biotite-  
1194 rich (red) Handegg shear zones differ from white mica-rich (blue) Oberaar  
1195 shear zones. Additionally one chlorite shear zone (green) is present.

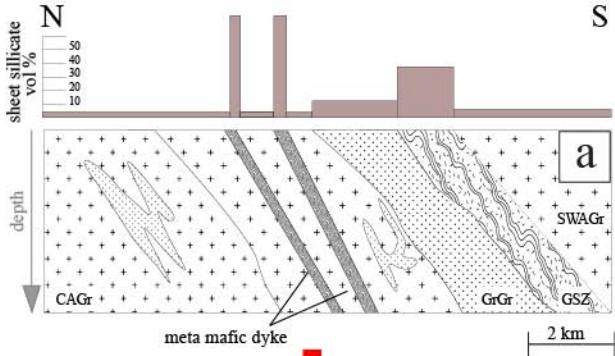
1196



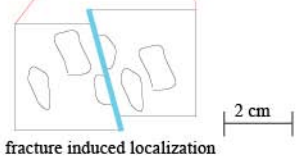
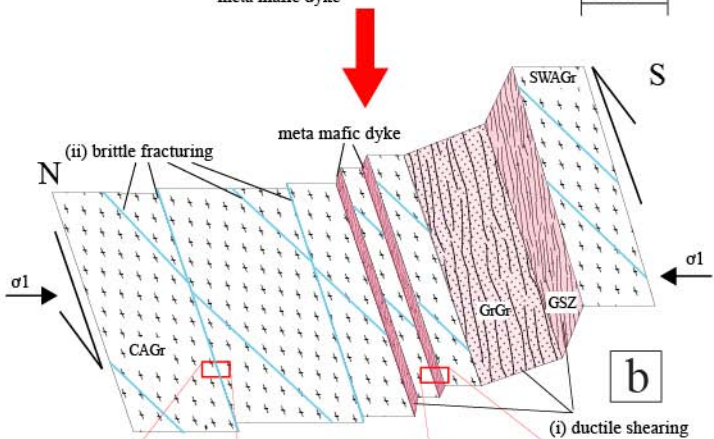




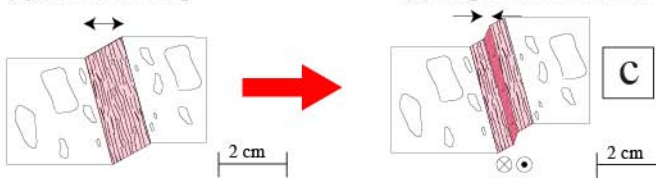
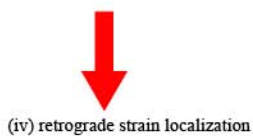
pre-Alpine  
anisotropies

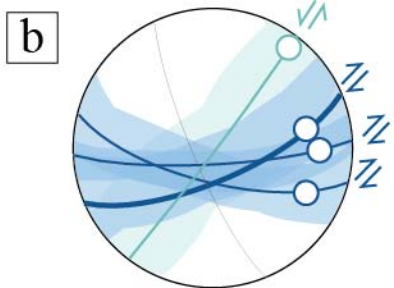
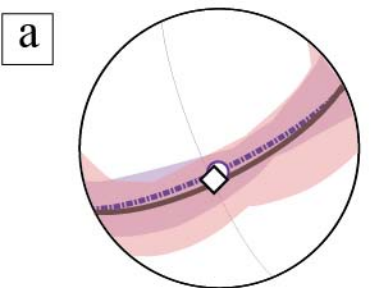


initiation of  
Alpine shear zones



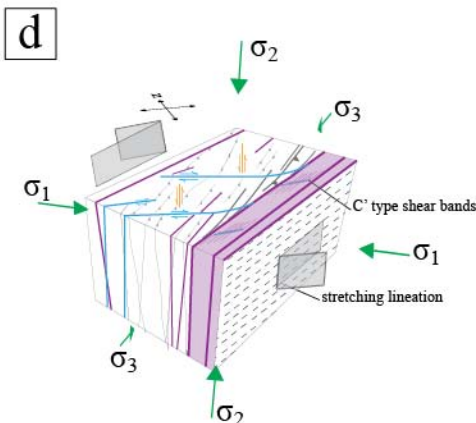
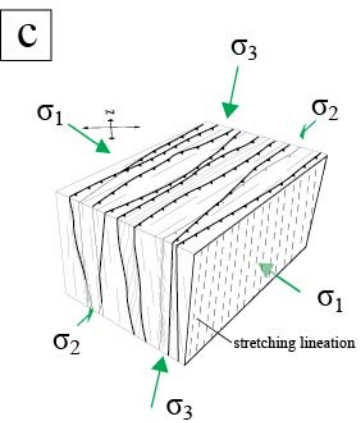
evolution of  
Alpine shear zone

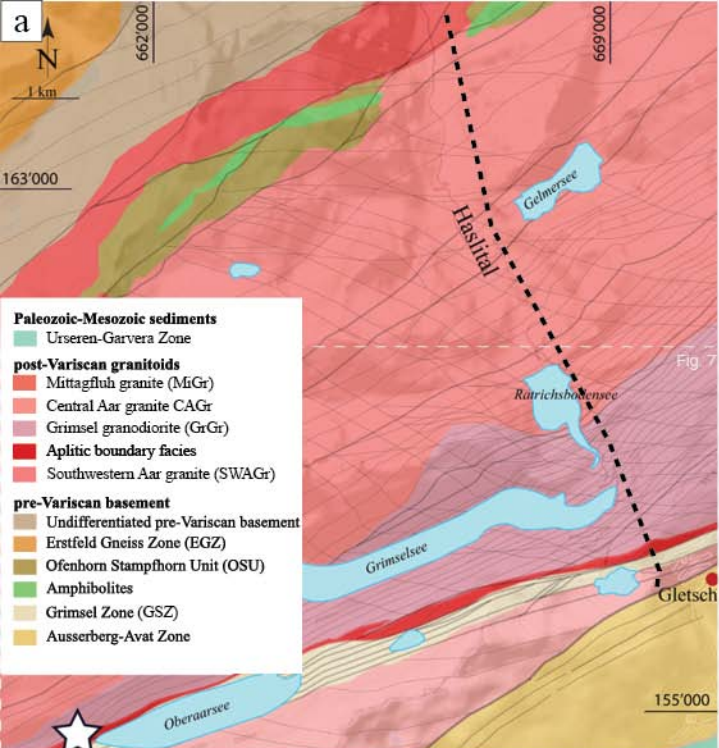




| great circles envelope | mean great circle | mean lineation |
|------------------------|-------------------|----------------|
| reverse shear zones    | —                 | —              |
| normal shear zones     | —                 | —              |

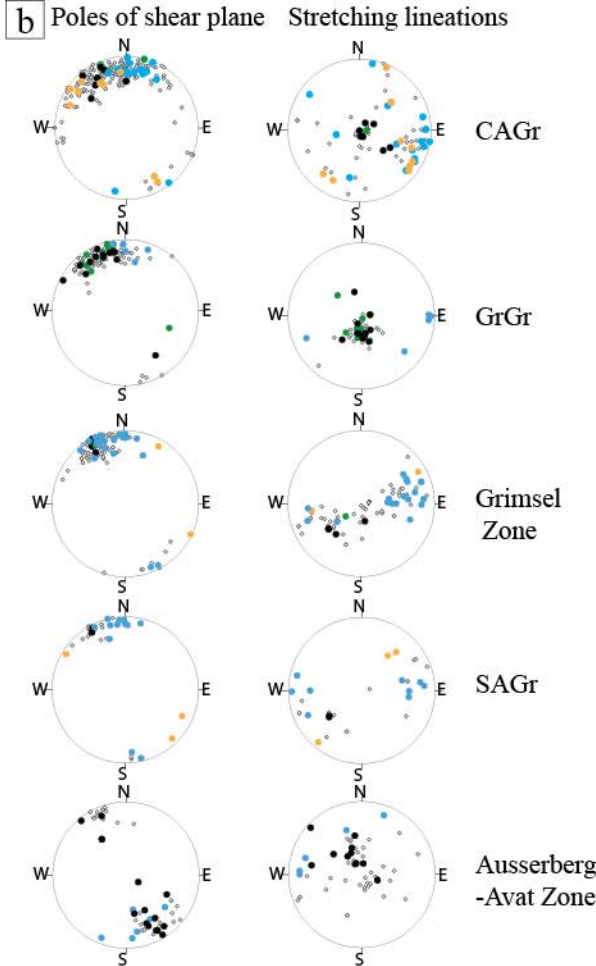
| great circles envelope   | mean great circle | mean lineation |
|--------------------------|-------------------|----------------|
| sinistral strike-slip sz | —                 | —              |
| dextral strike-slip sz   | —                 | —              |





- shear zone
- major shear zone
- ☆ Oberaar mapping (Fig. 10)
- - - approximate trace of the Transitgas tunnel

- unknown shear sense
- reverse shear sense
- normal shear sense
- dextral shear sense
- sinistral shear sense



Host rock (bkg)

High strain zone (sz)

Sheet silicate content (vol%)

10 20 30 40 50 60 70 80 90

CAGr



a



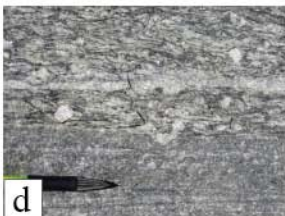
b



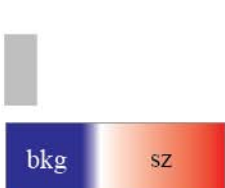
GrGr



c



d



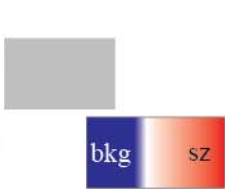
Grimmel Zone



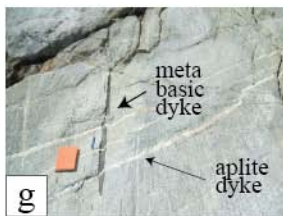
e



f



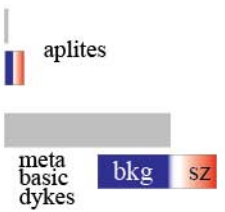
magmatic dyke



g



h



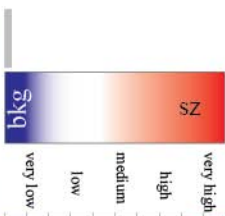
SWAGr



i



j

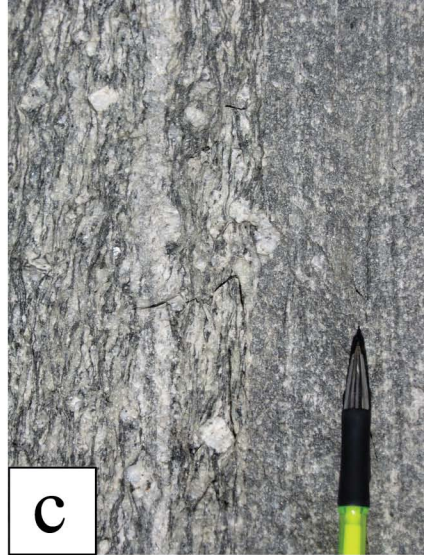
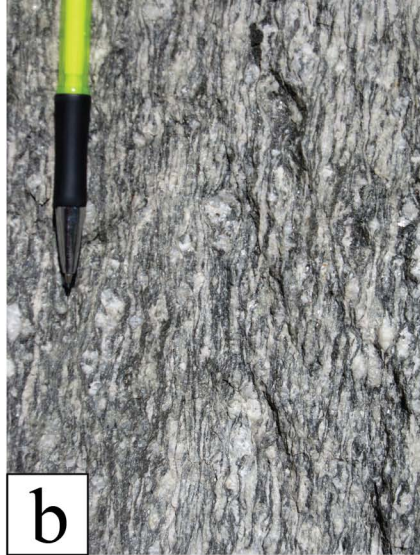


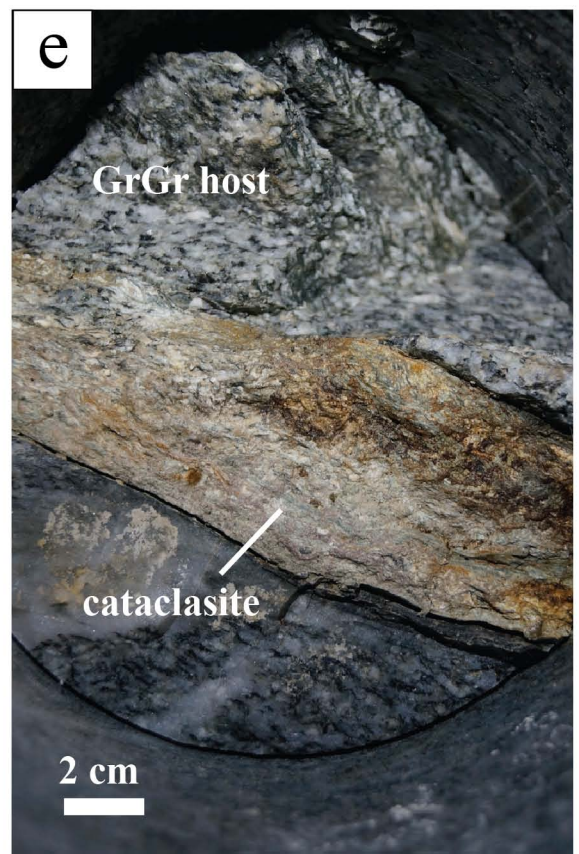
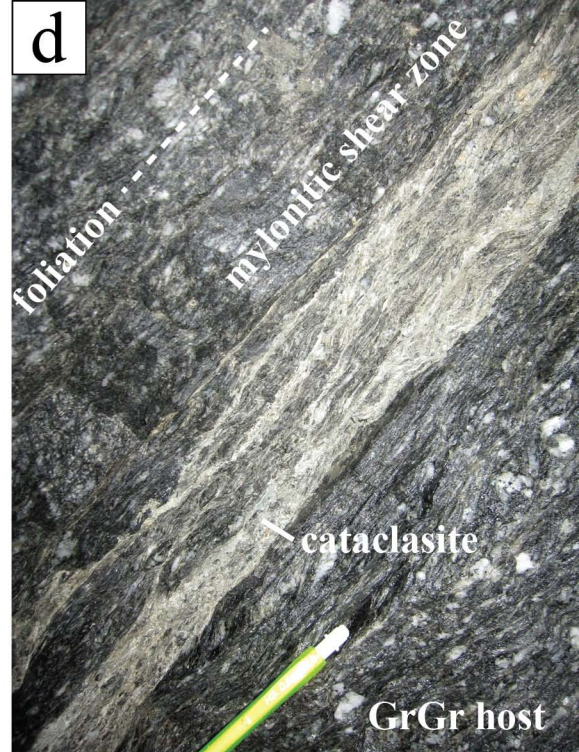
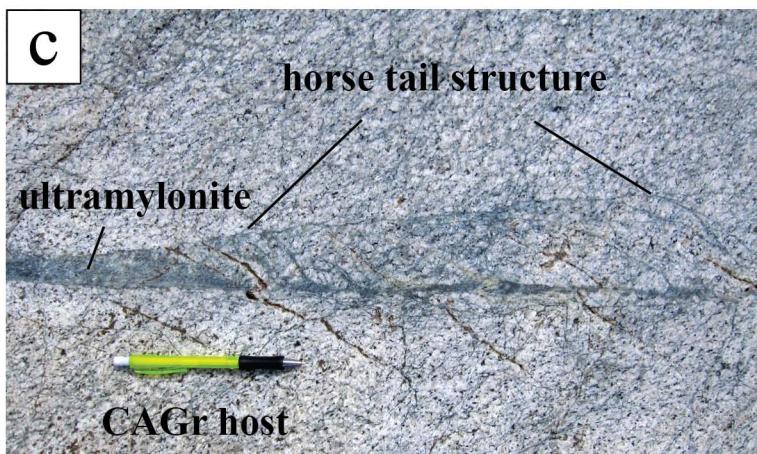
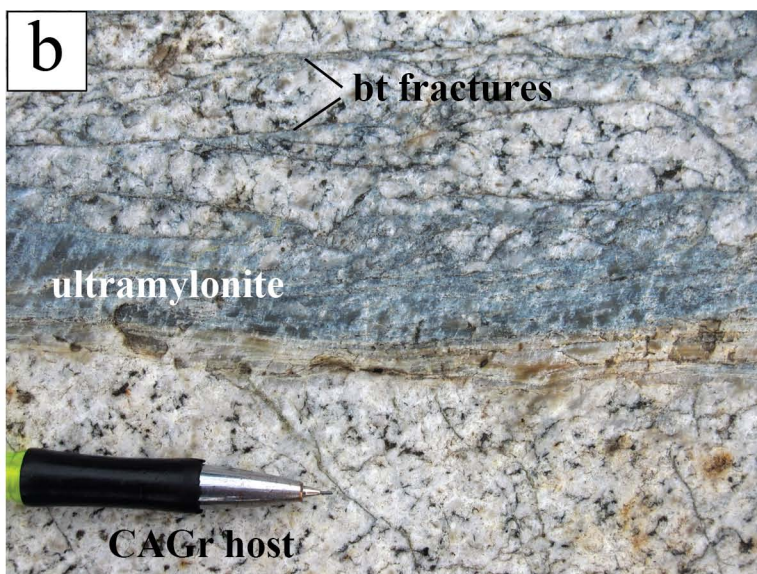
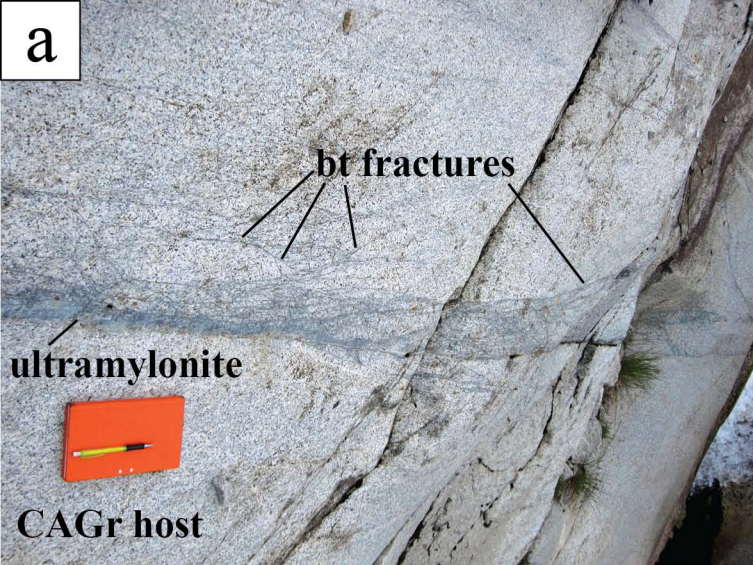
Host rock (bkg)

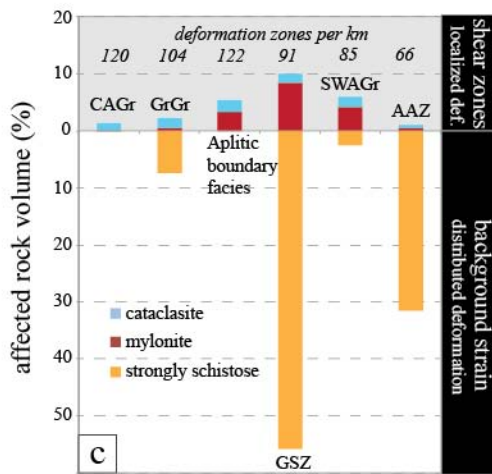
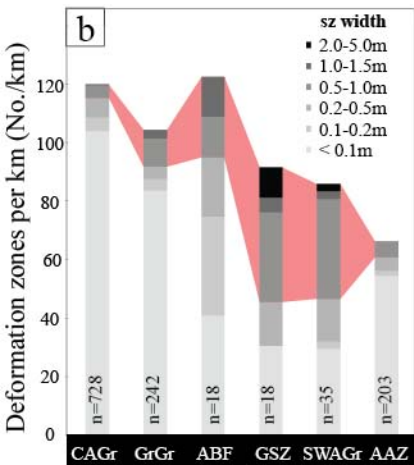
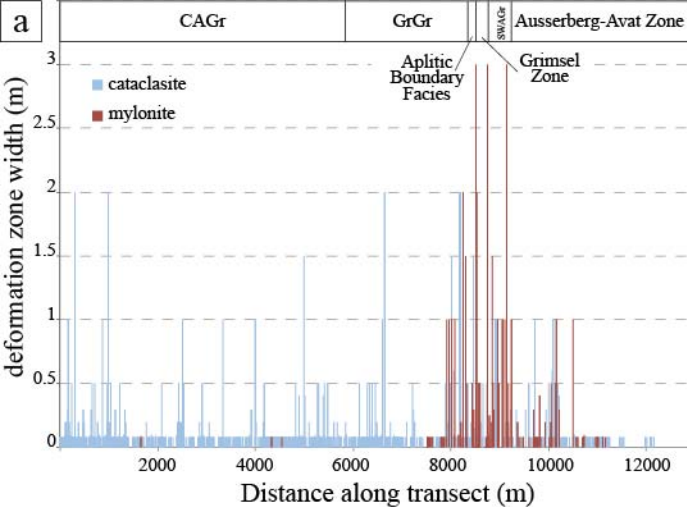
High strain zone (sz)

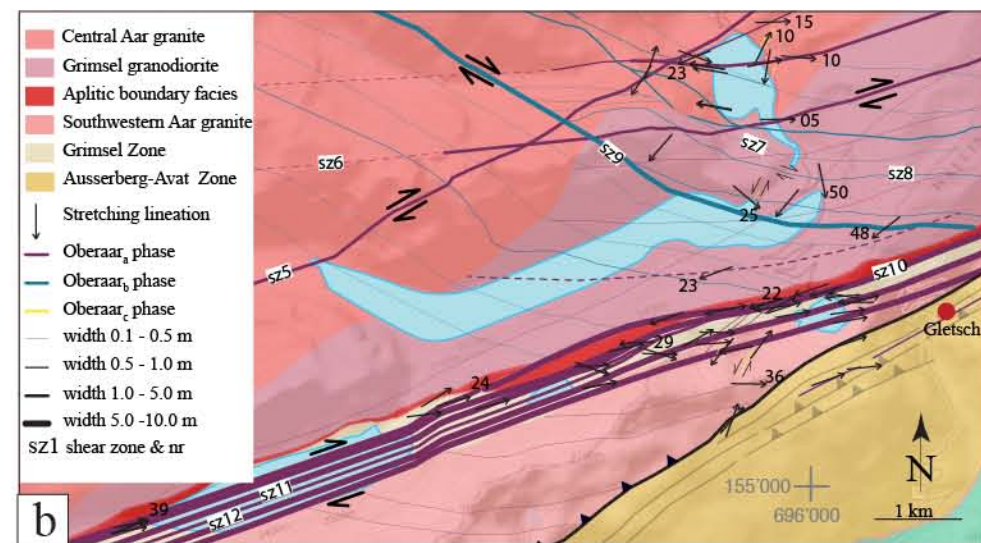
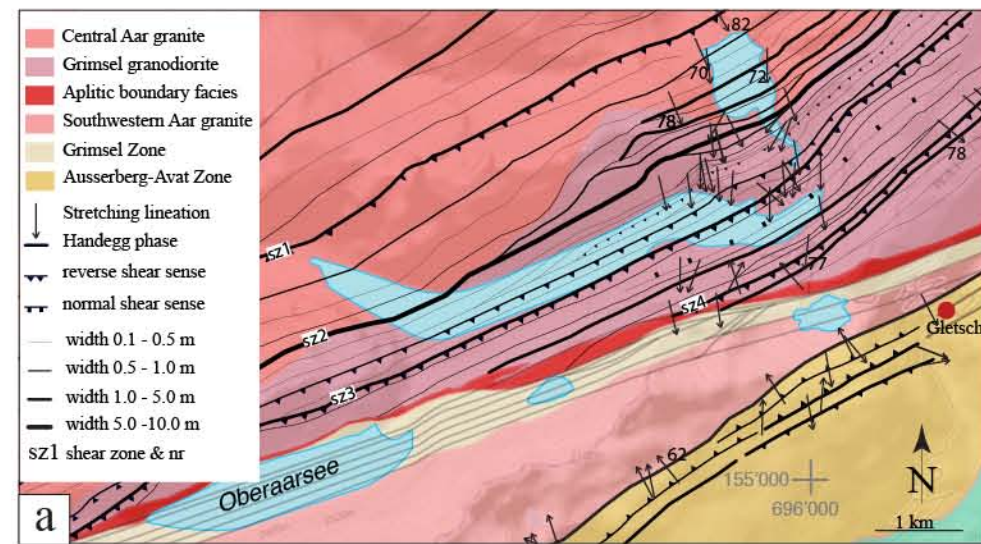
Strain intensity

very low low medium high very high





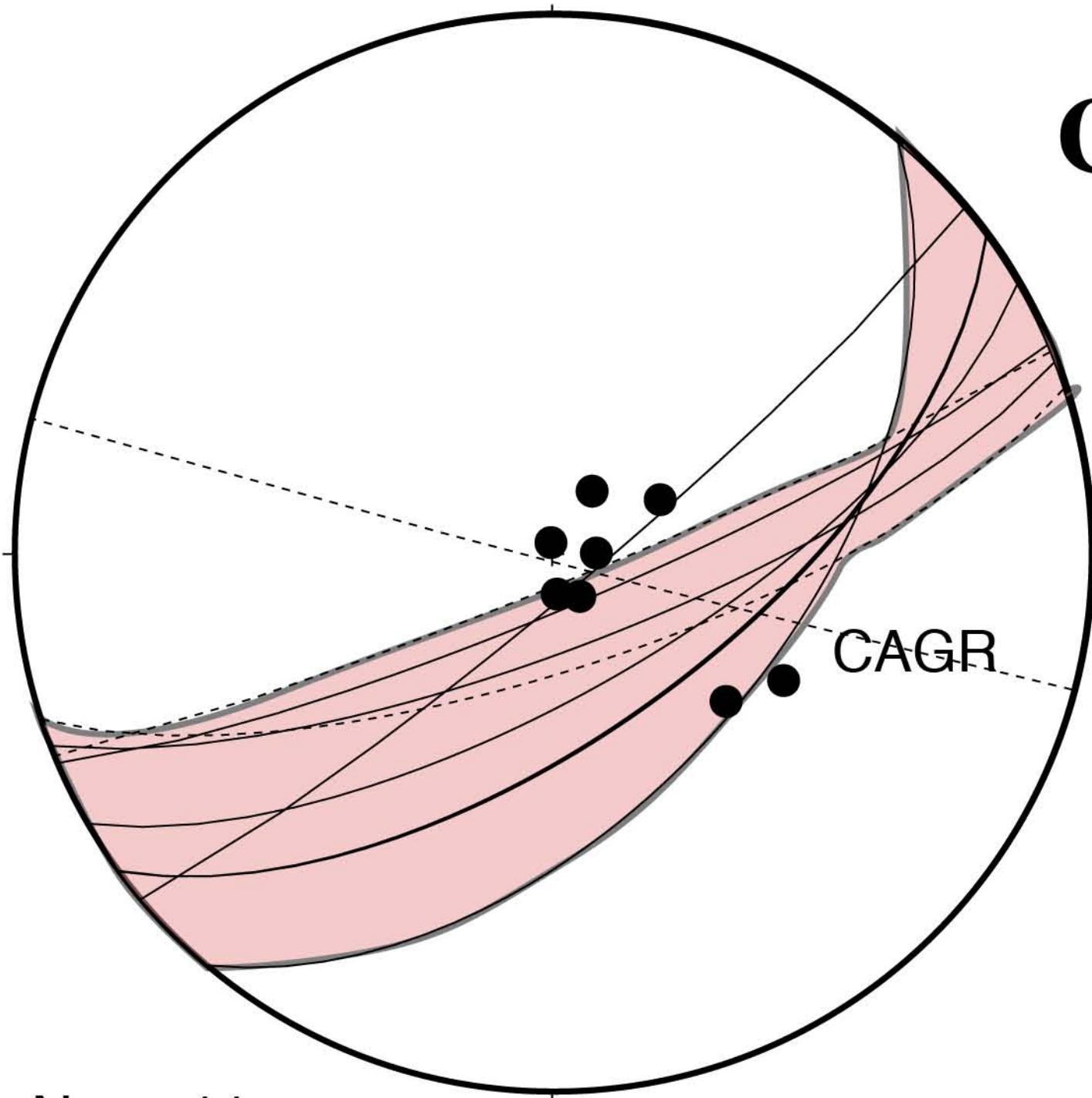




**Handegg phase**  
reverse-normal shearing

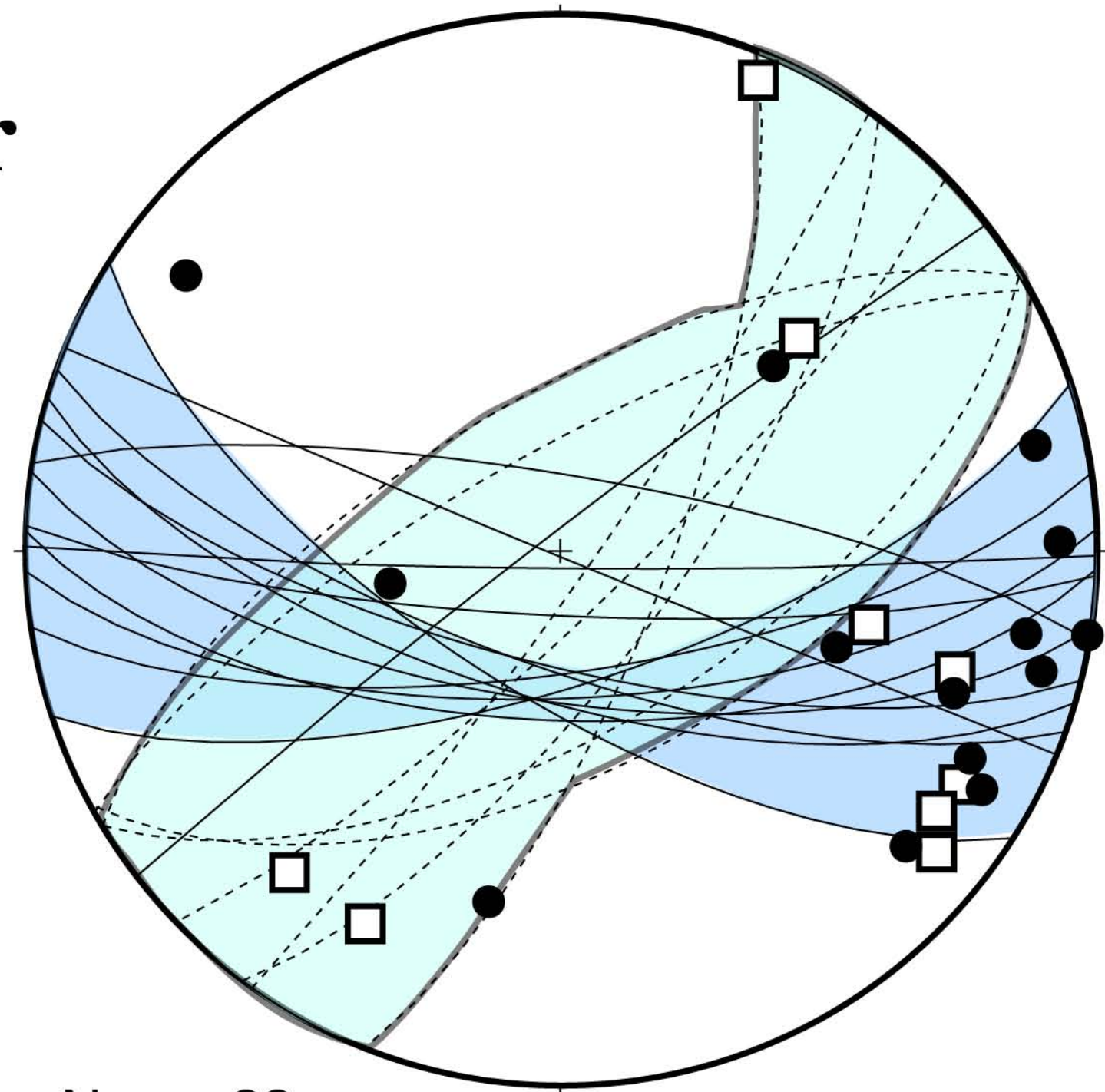
**Oberaar phase**  
strike-slip shearing

**CAGr**



$N_{SZ} = 11$

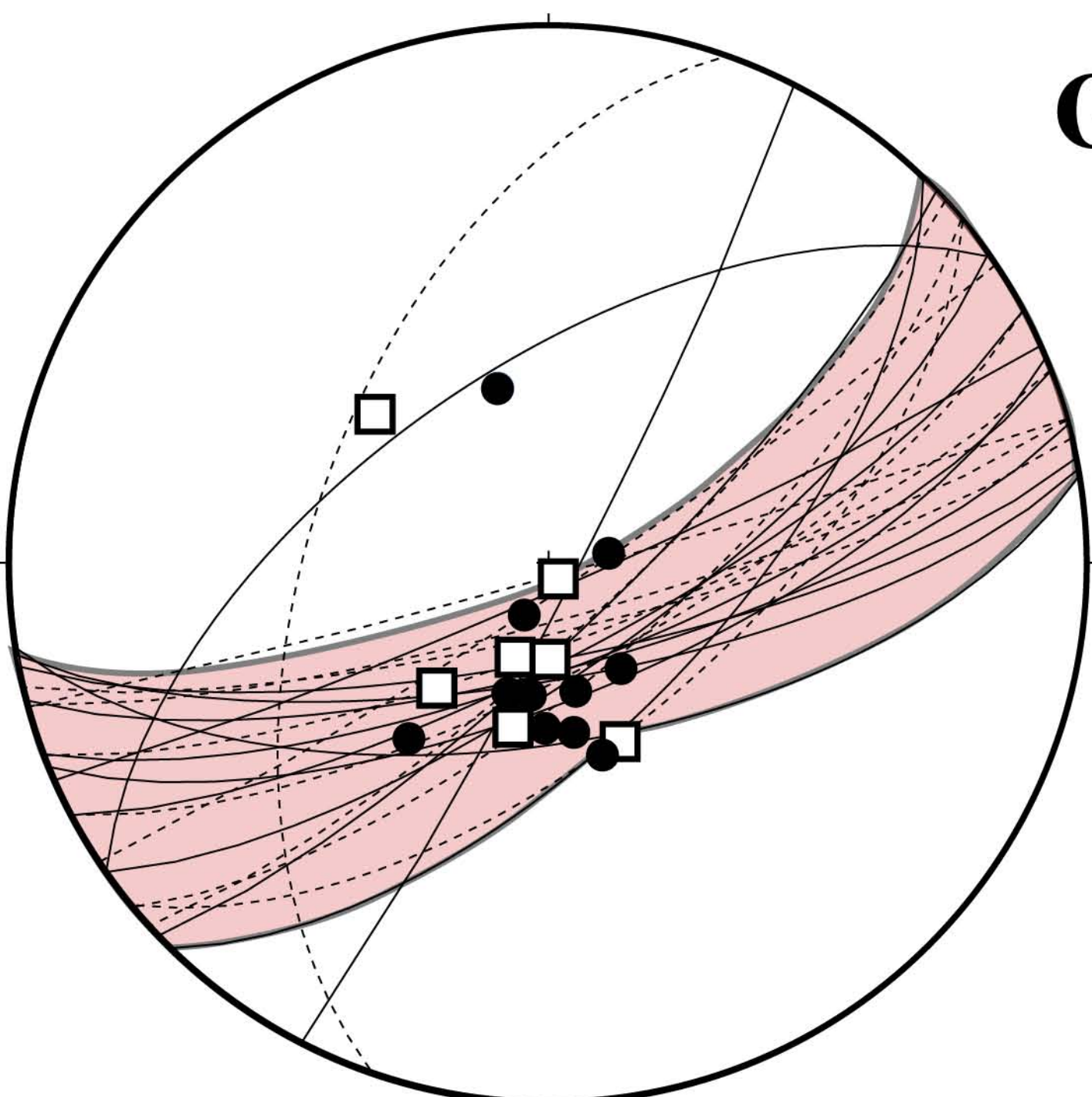
$N_L = 8$



$N_{SZ} = 22$

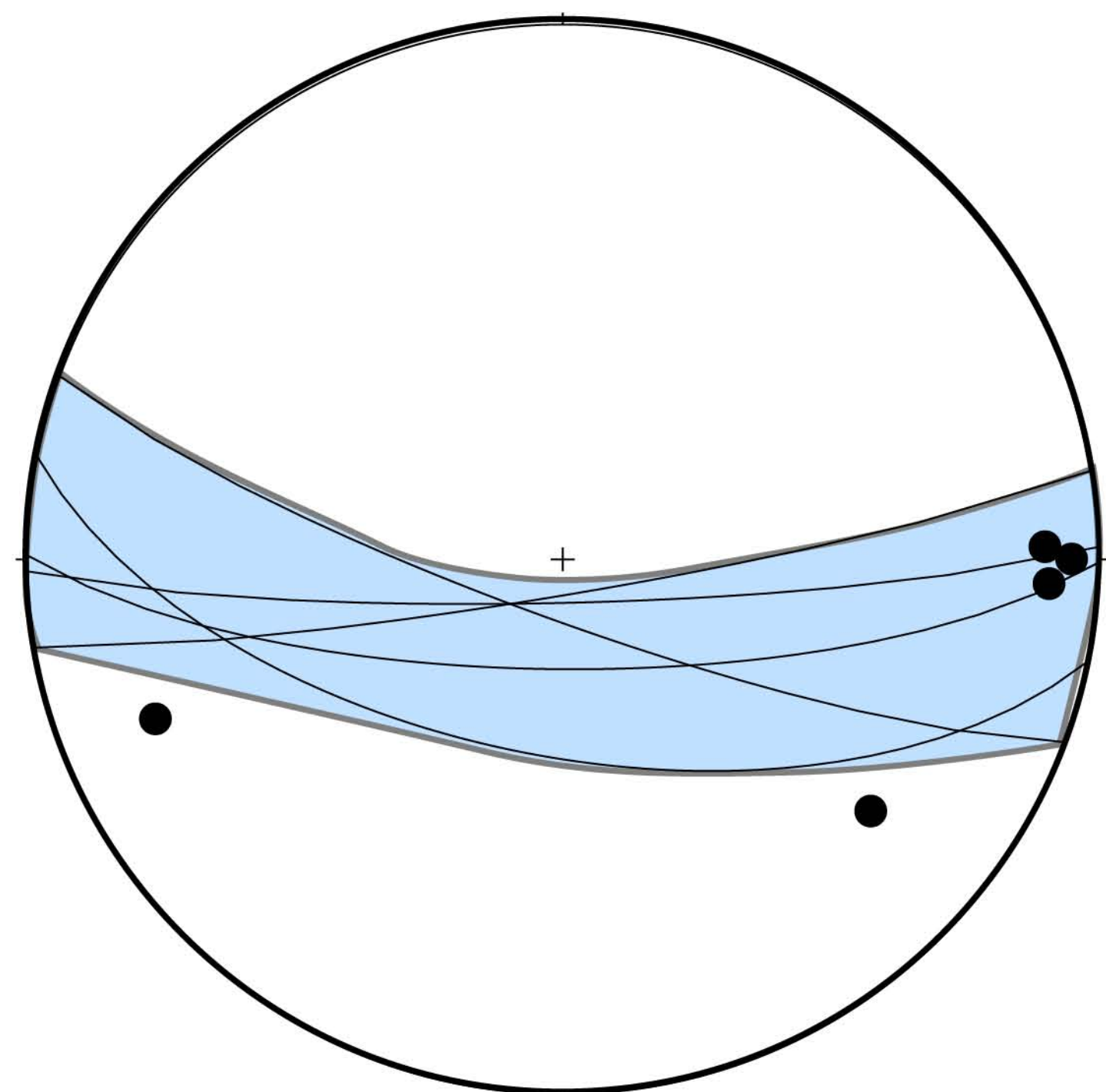
$N_L = 23$

**GrGr**



$N_{SZ} = 23$

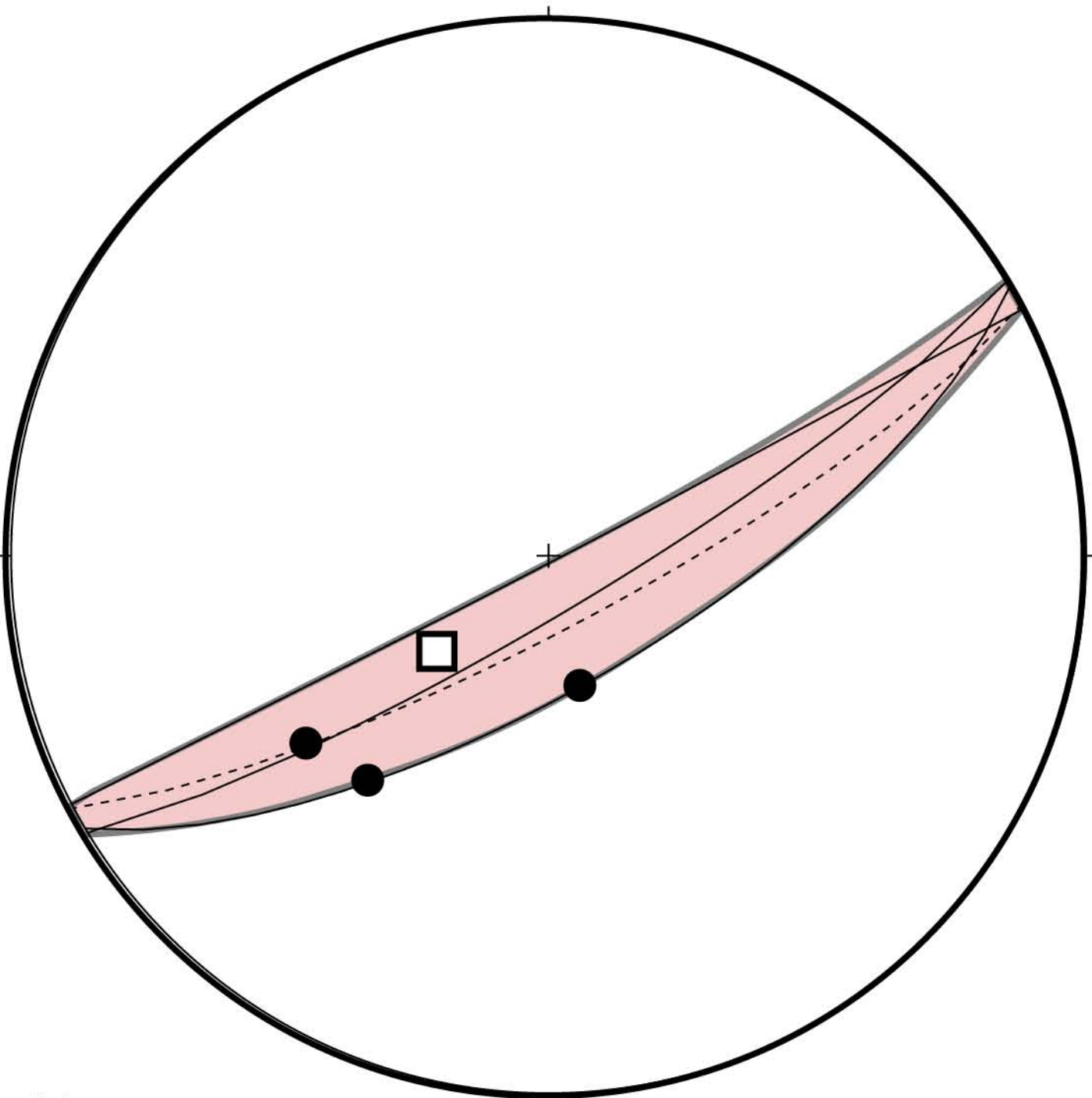
$N_L = 18$



$N_{SZ} = 5$

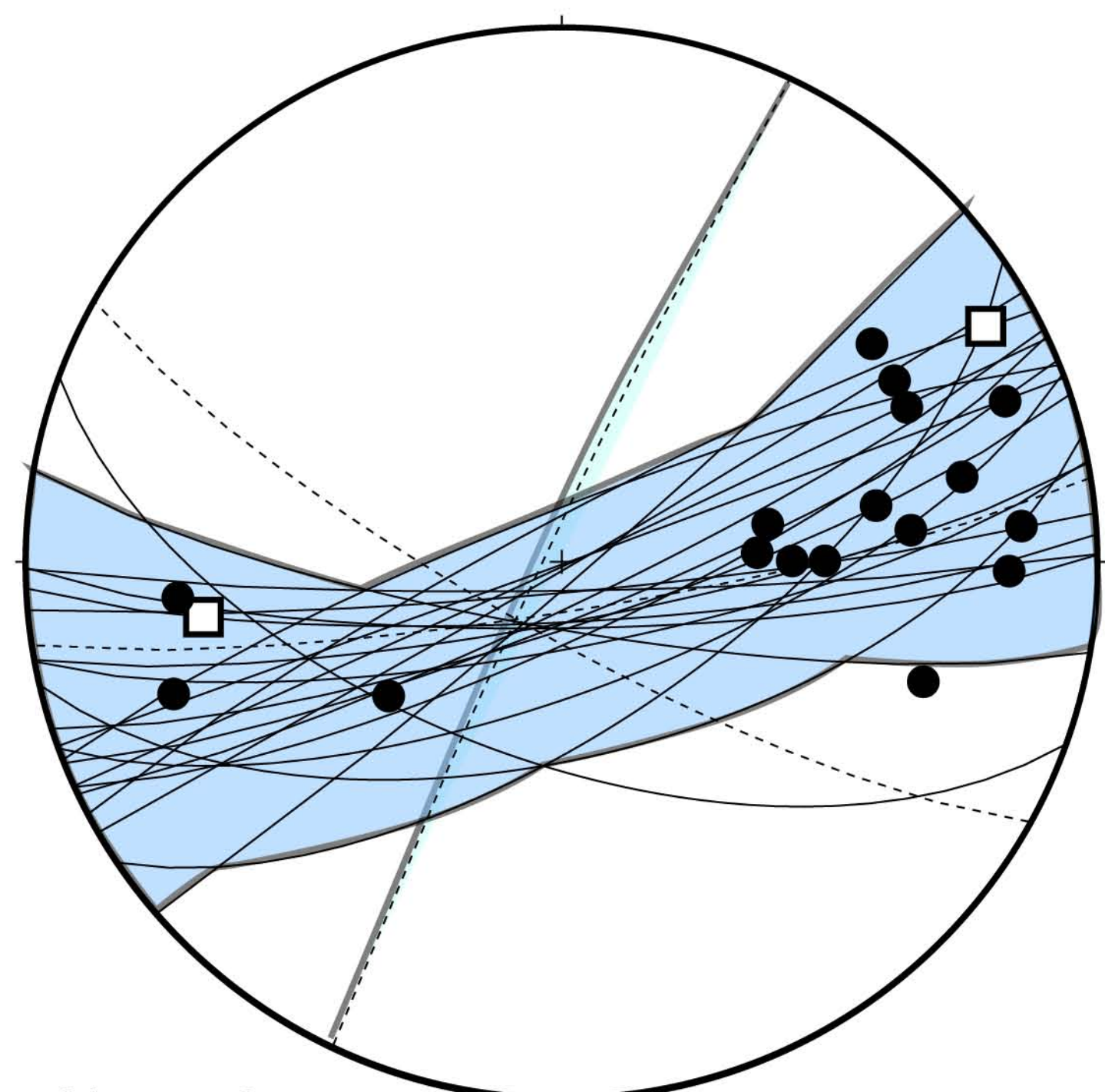
$N_L = 5$

**GSZ**



$N_{SZ} = 4$

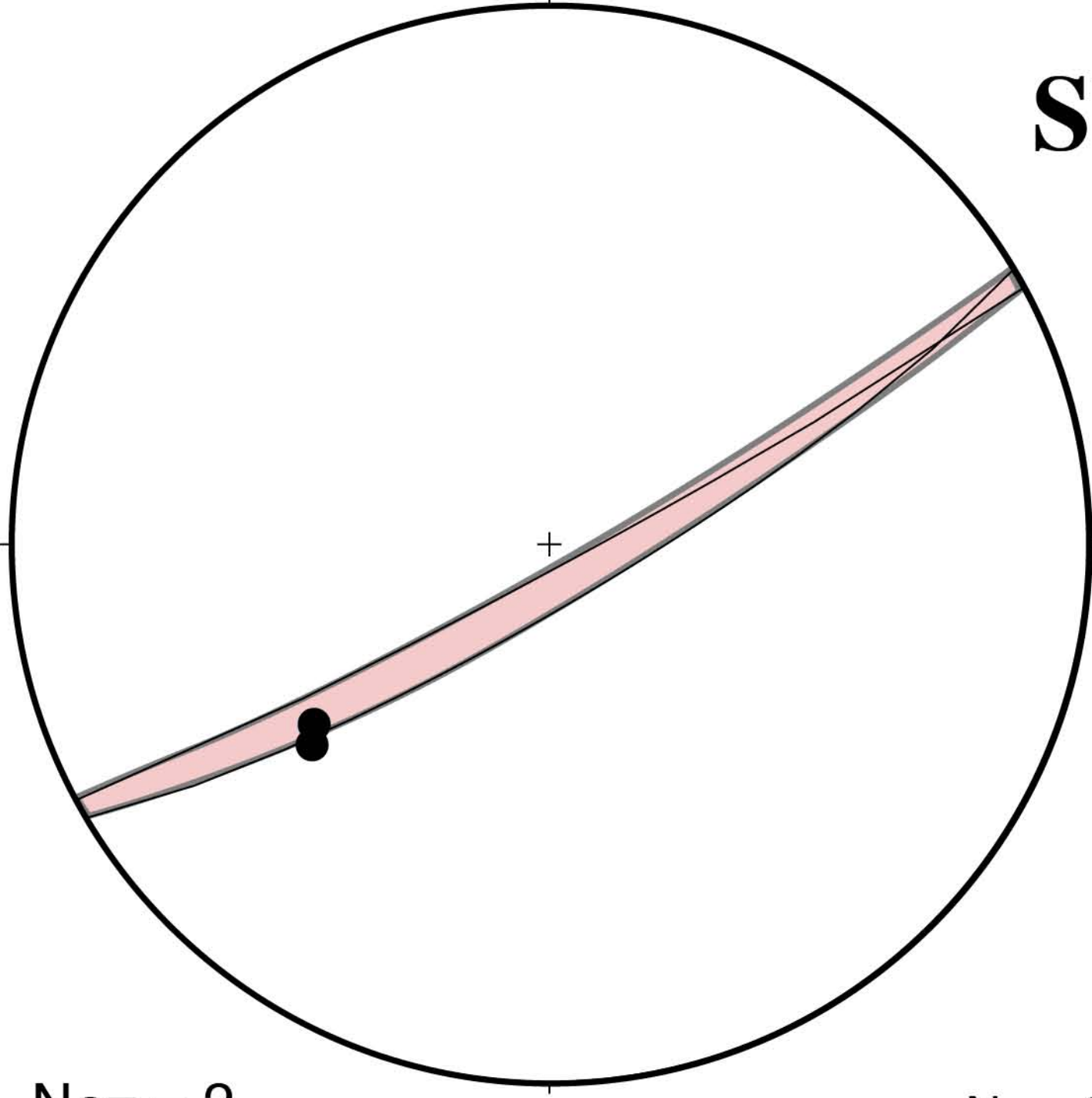
$N_L = 4$



$N_{SZ} = 24$

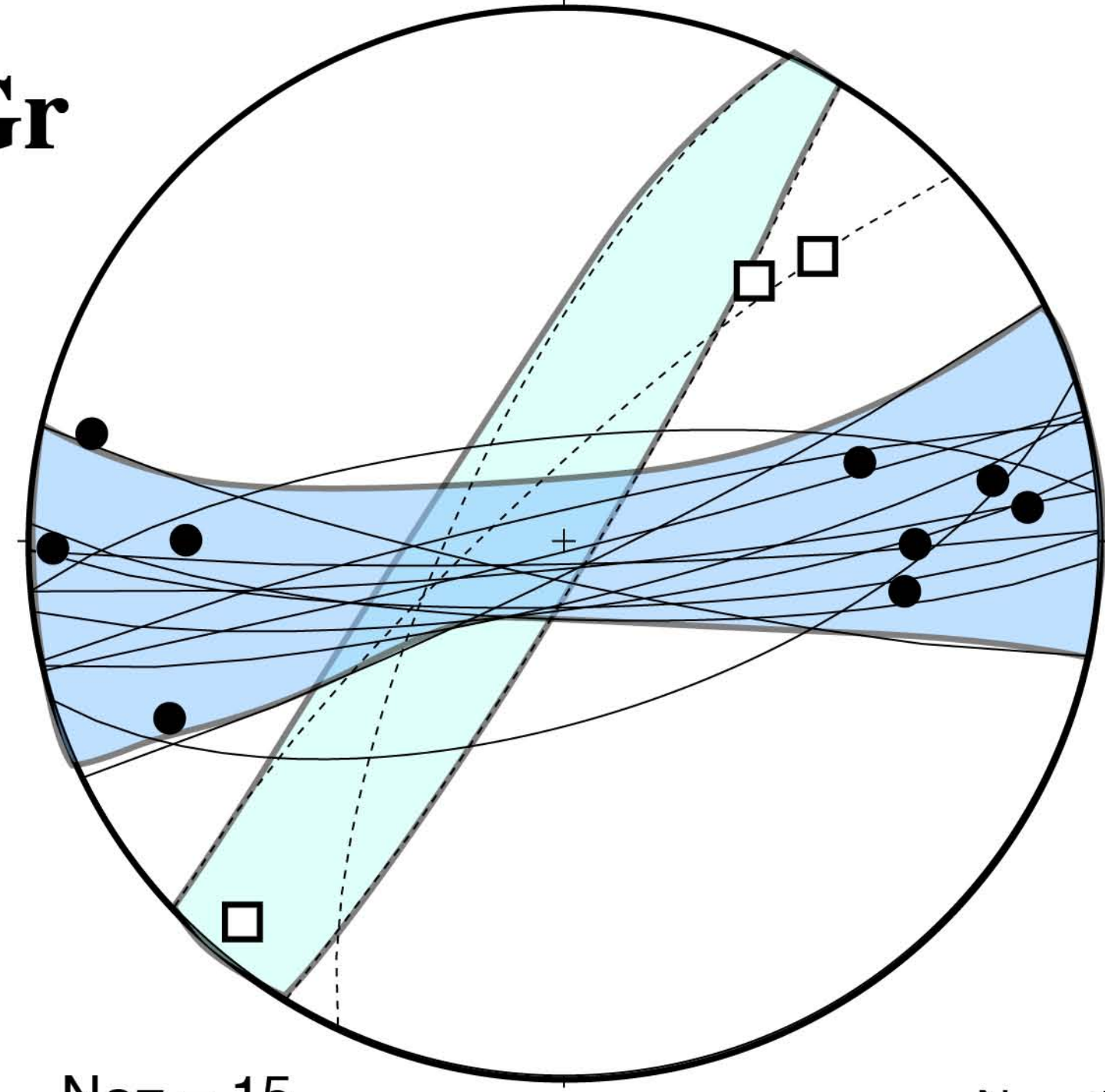
$N_L = 19$

**SWAGr**



$N_{SZ} = 2$

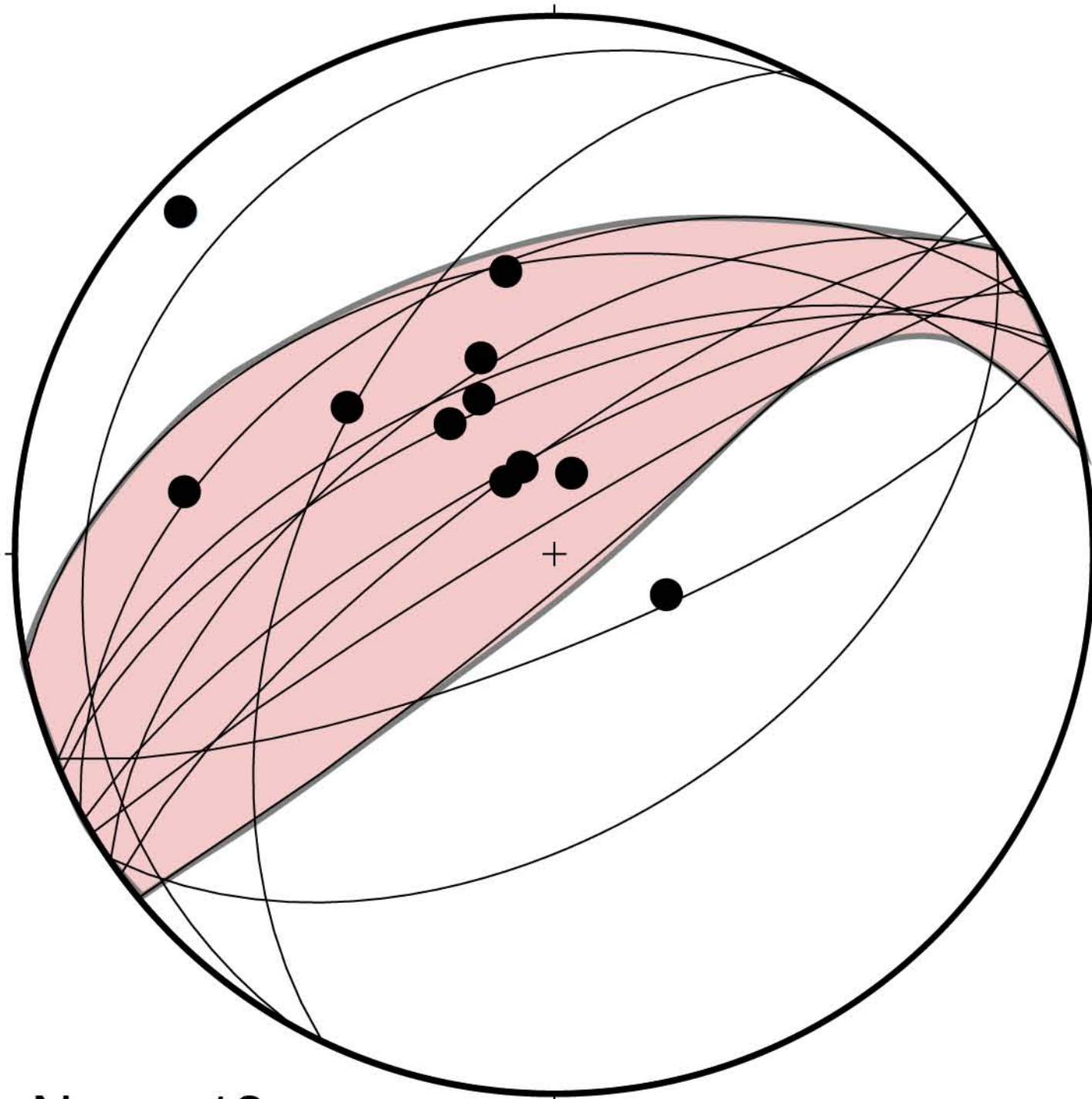
$N_L = 2$



$N_{SZ} = 15$

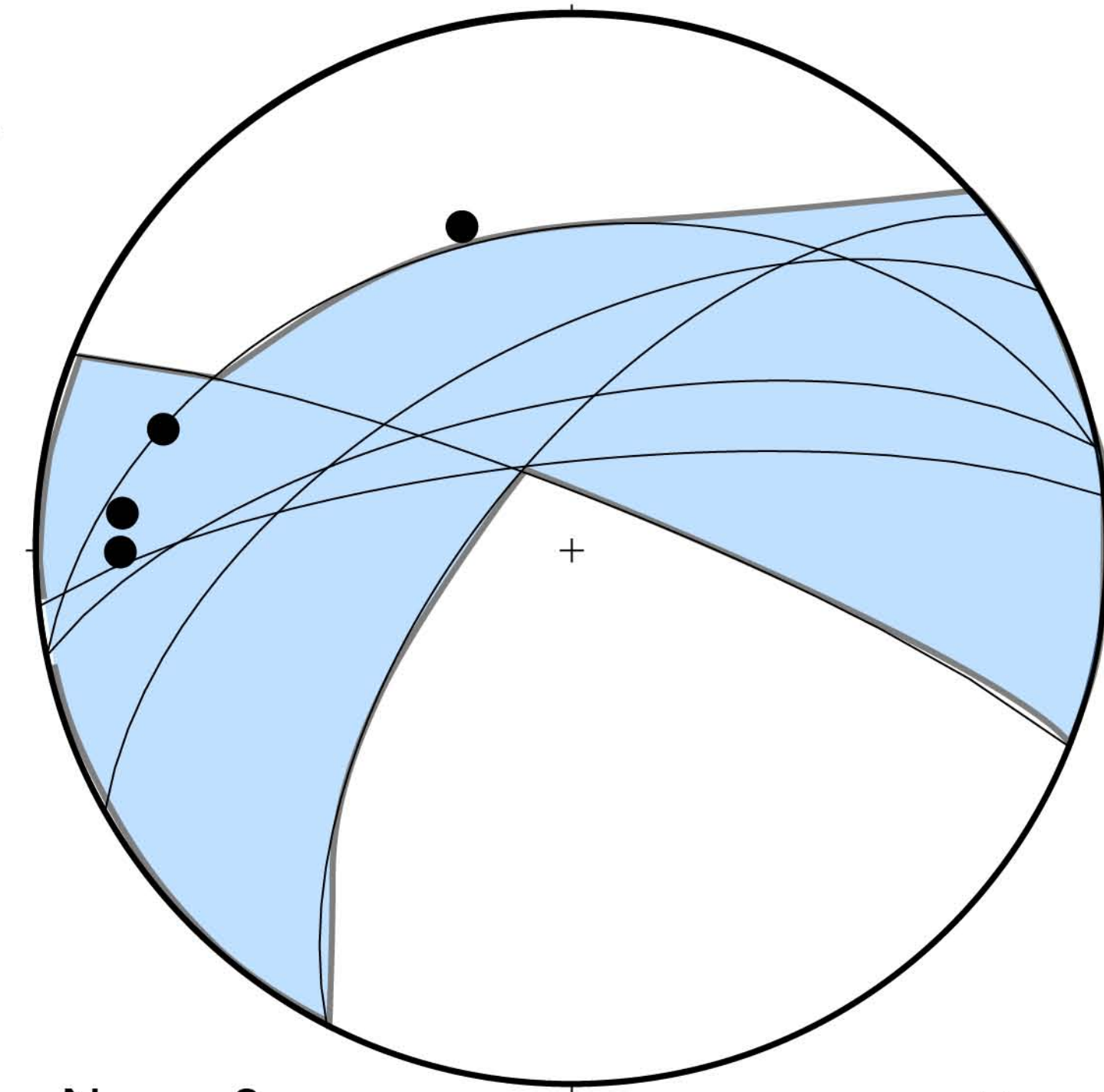
$N_L = 12$

**AAZ**



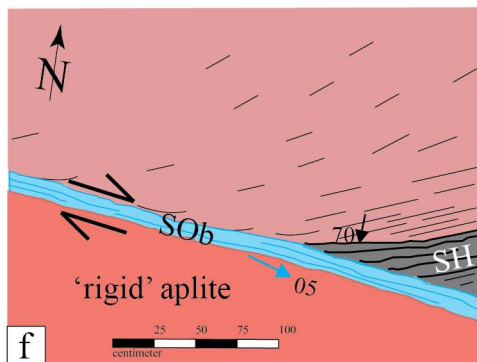
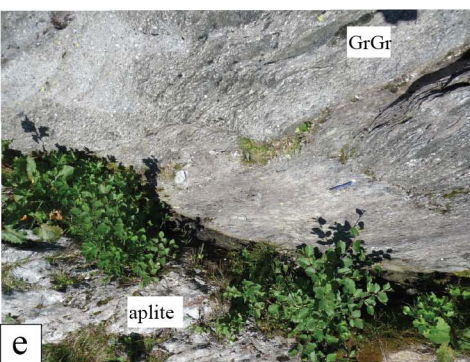
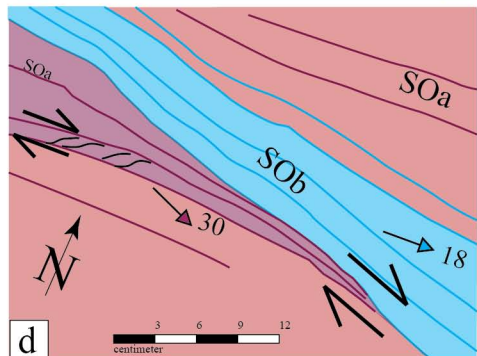
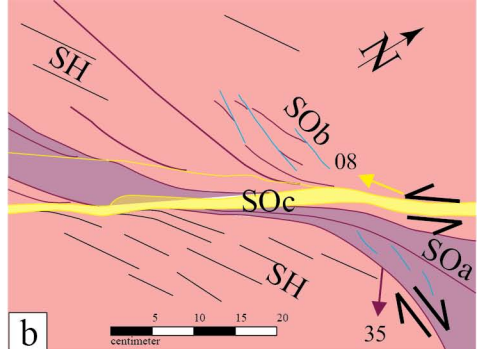
$N_{SZ} = 13$

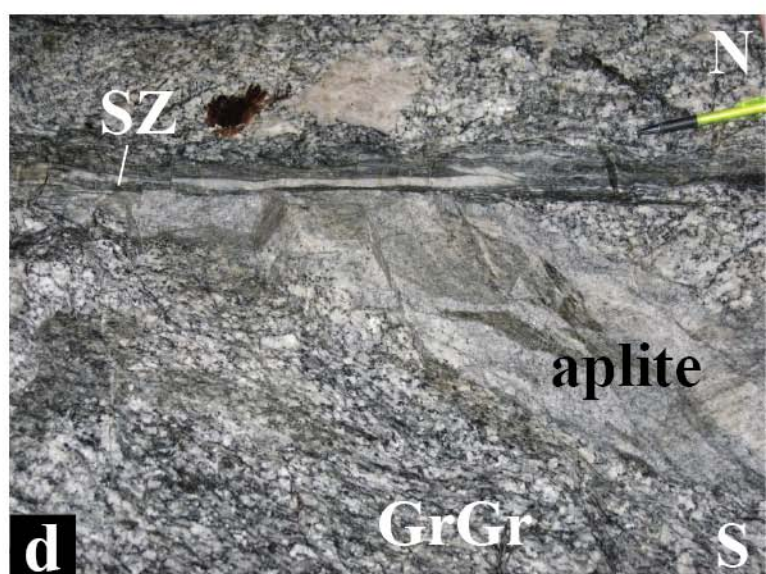
$N_L = 11$



$N_{SZ} = 6$

$N_L = 4$





Supplementary Figure

## Captions of supplementary figures

### Fig. A

Photograph showing km-scale steep, S-dipping Handegg phase shear zones (red lines) in the Alplistock-Ärlenhoren area (665°000/161°000). Note the major shear zones being connected by shorter secondary ones.

### Fig. B

Handegg phase shear zones in aplitic boundary facies at the outcrop scale (locality: 668°942/157°321). (a) Steep S-dipping main set of Handegg shear zones (hanging wall up toward N) being interconnected by secondary set of steep N-dipping Handegg shear zones with opposite sense of shear (hanging wall up toward S). (b) and (c) indicate positions of corresponding figures. (b) Steep main Handegg shear plane with stretching lineations, rotating from down dip to an oblique slip, documenting the transition from reverse Handegg phase to oblique Oberaar phase shearing. (c) Steep secondary N-dipping Handegg phase shear plane with hanging wall up toward S sense of shear. Fieldbook (20x13 cm) and pen (diameter 7 mm) as a scale.

Fig. C. Handegg phase shear zones in aplitic boundary facies at the outcrop scale (locality 668°934/157°341). (a) overview image showing two subvertical mylonitic main shear zones (1,2) being connected by secondary mylonitic shear zone branches (3, 4). Main and secondary shear zones form a conjugate set with opposite shear senses. Orientations of shear planes and stretching lineations of (1) and (2) are (Sz1: 347/88, Sz2: 195/87) and (SL1: 295/63, SL2: 277/73), respectively. Orientations of shear planes and stretching lineations of (3) and (4) are (Sz3: 342/70, Sz4: 355/66) and (SL3: 302/66, SL4: 321/56), respectively. (b) Enlarged view of (a) showing the mylonitic foliation within the Handegg phase secondary shear zone branch (4) Fieldbook as a scale, 20x13 cm.

### Fig. D

Crosscutting relationships between Handegg und Oberaar phase. (a) Large-scale relationship showing NE-SW striking Handegg shear zone ( $Sz_{Ha}$ ) being cut by younger Oberaar phase shear zones (large-scale dextral  $Sz_{10}$  Oberaar<sub>a</sub> ( $Sz_{Oba}$ ) and dextral Oberaar<sub>b</sub> ( $Sz_{Obb}$ )). Image shows area around location 668°000/158°000. (b) Bird's eye view of a granodiorite dissected by an aplite dyke (Ap) with pervasive Handegg phase foliation ( $S_{Ha}$ ) all being cut by a dextral Oberaar<sub>a</sub> ( $Sz_{Oba}$ ) shear zone. (c) Enlarged detail from (b) illustrating the presence of a 1cm wide mylonitic fabric in the Oberaar<sub>a</sub> ( $Sz_{Oba}$ ) shear zone. Outcrop locality: 669°250/157°275.

### Fig. E

Crosscutting relationship Handegg phase and Oberaar<sub>c</sub> shear zone. (a) Sinistral Oberaar<sub>c</sub> shear zones crosscutting at high angle a W-E striking metabasic dyke (mbd, nagra Grimsel Test Side). (b) E-W striking Metabasic dyke being being strongly deformed during Alpine shearing. (c,d) Bird's eye view of Grimselgranodiorite and aplite dykes (Ap) with pervasive Handegg phase background foliation ( $S_{Ha}$ ) being dissected by a sinistral Oberaar<sub>c</sub> strike-slip shear zone ( $Sz_{Obc}$ ). (c) overview figure

with 8 cm long pocket knife as scale. Inset shows position of enlargement in (d).  
Outcrop locality: 668°150/157°140.

Fig. F.

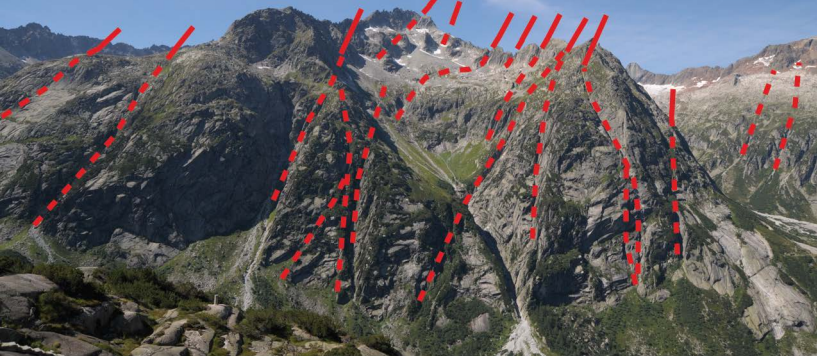
Compilation of shear plane orientations, stretching lineations and shear senses for Handegg and Oberaar-c structures collected within a one kilometer wide stripe parallel to the profile section P-P' (for location of profile trace see F in Fig. 7b). (a) Vertical cross section with major shear zones (grey and rock types). (b) Geological map with plunge azimuth of stretching lineations. (c) Changes in plunge for the different stretching lineations. (d) Changes in dip azimuth of the different shear planes. CAGr: Central Aar granite, GrGr: Grimsel granodiorite, APF: aplitic boundary facies, GZ: Grimsel zone, SWAGr: southwestern Aar granite, AAZ: Ausserberg-Avat zone, GSPZ: Grimselpass shear zone.

S

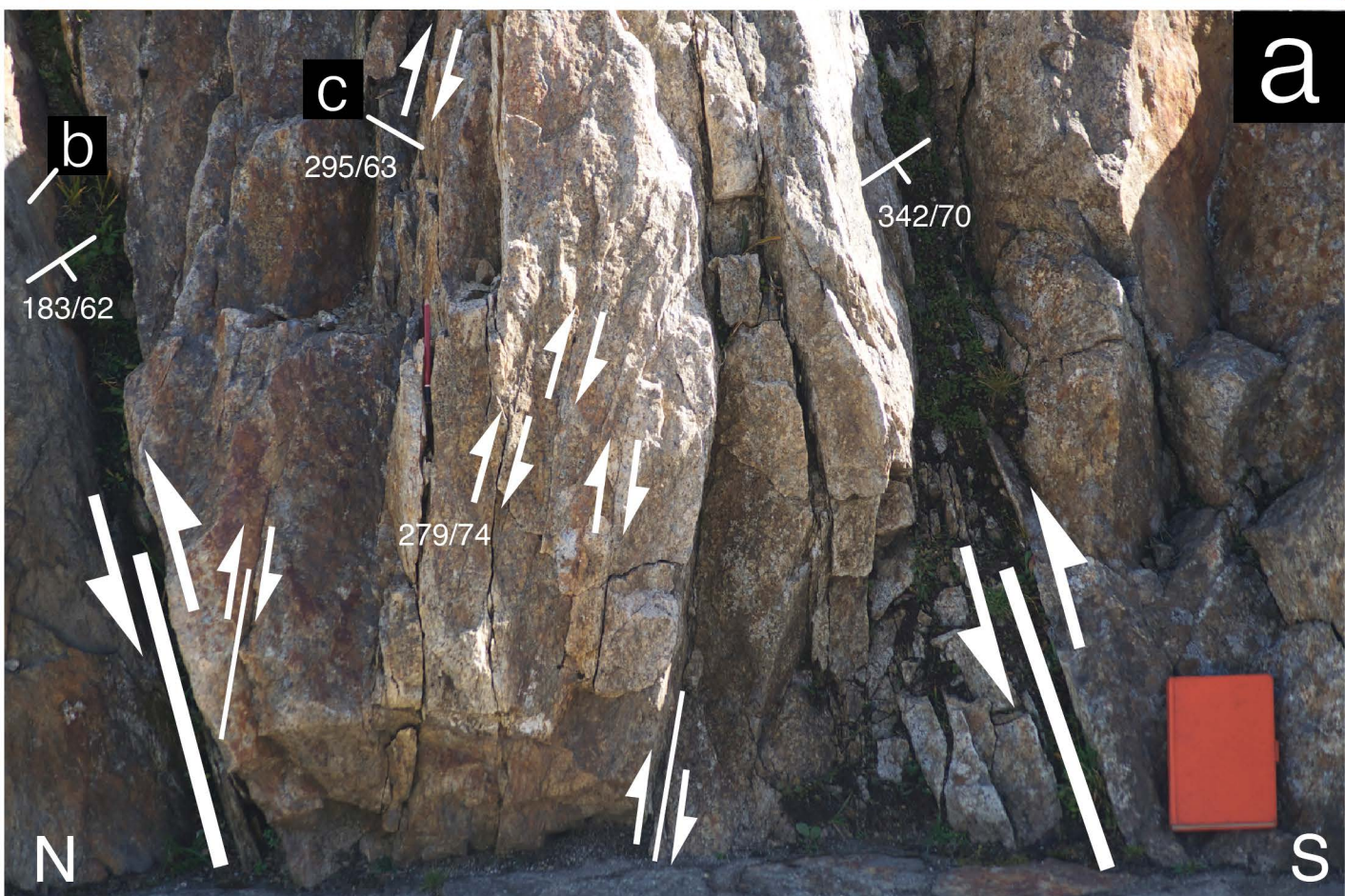
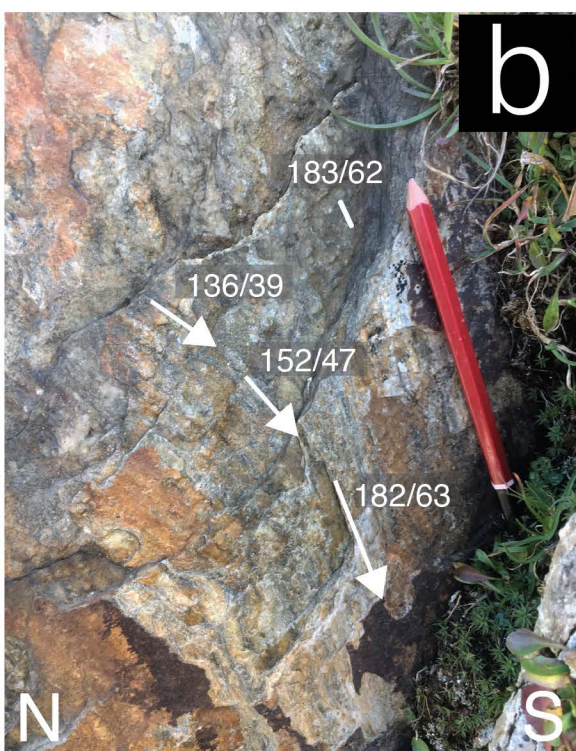
N

Alplistock

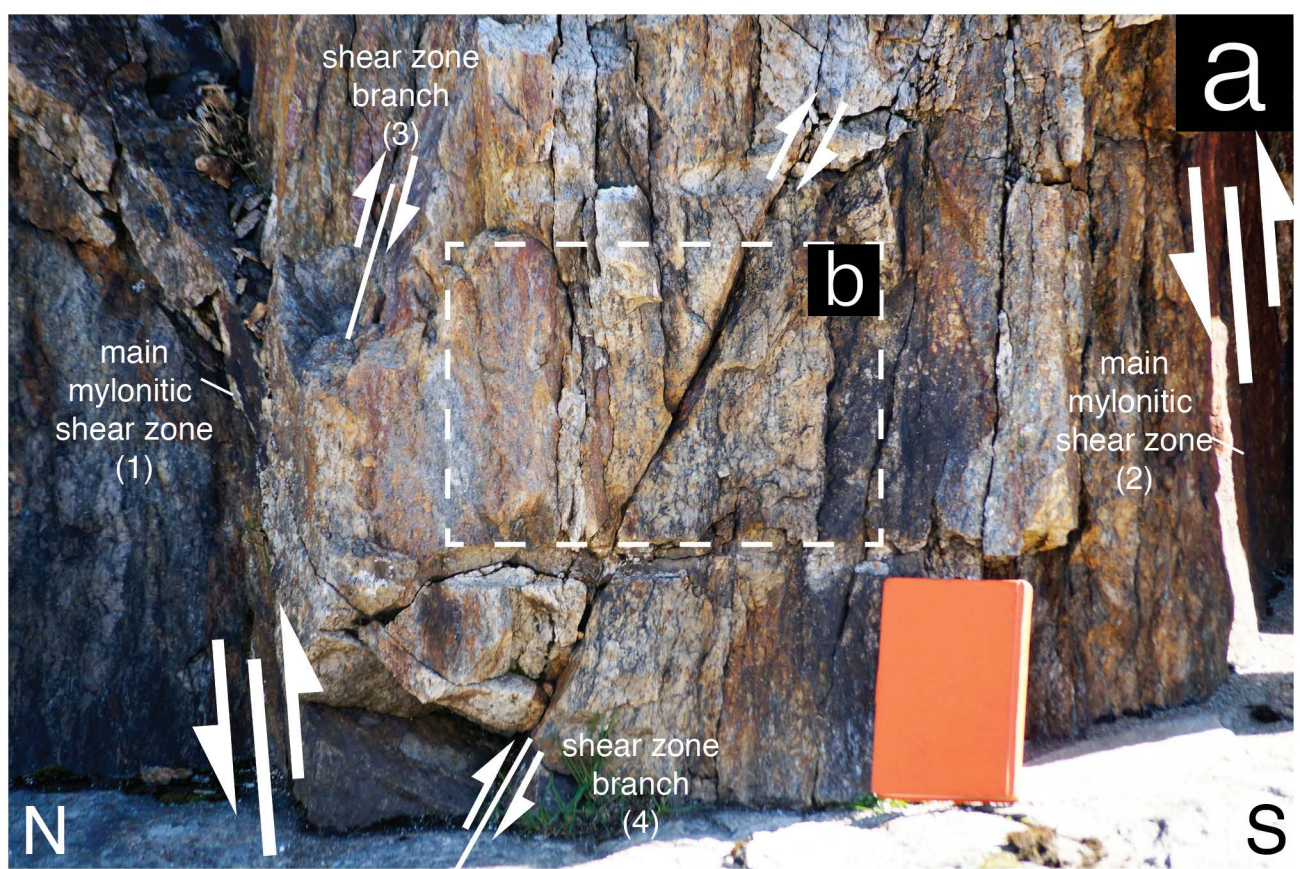
Ärlenhoren



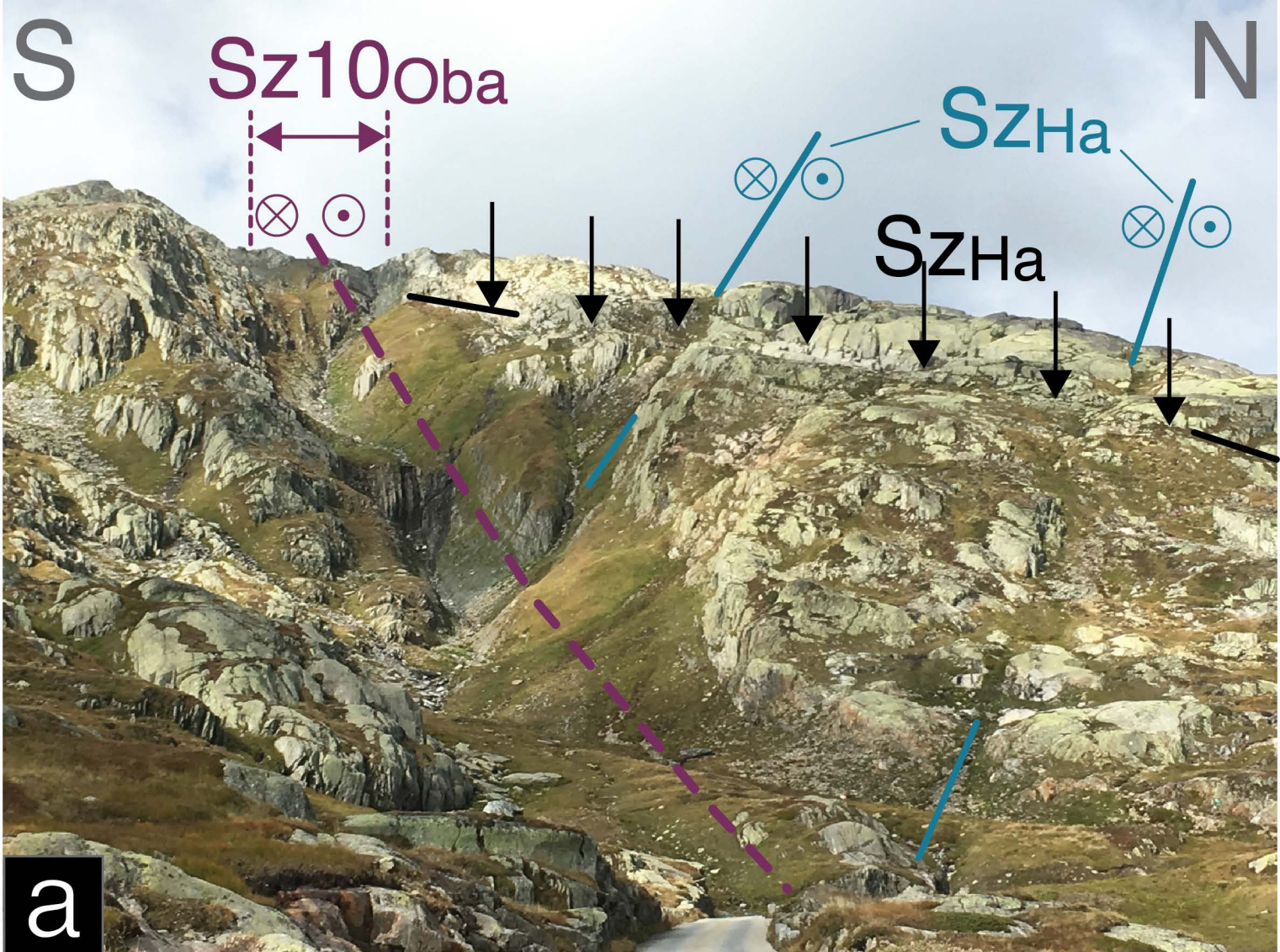
Supplementary Fig. A



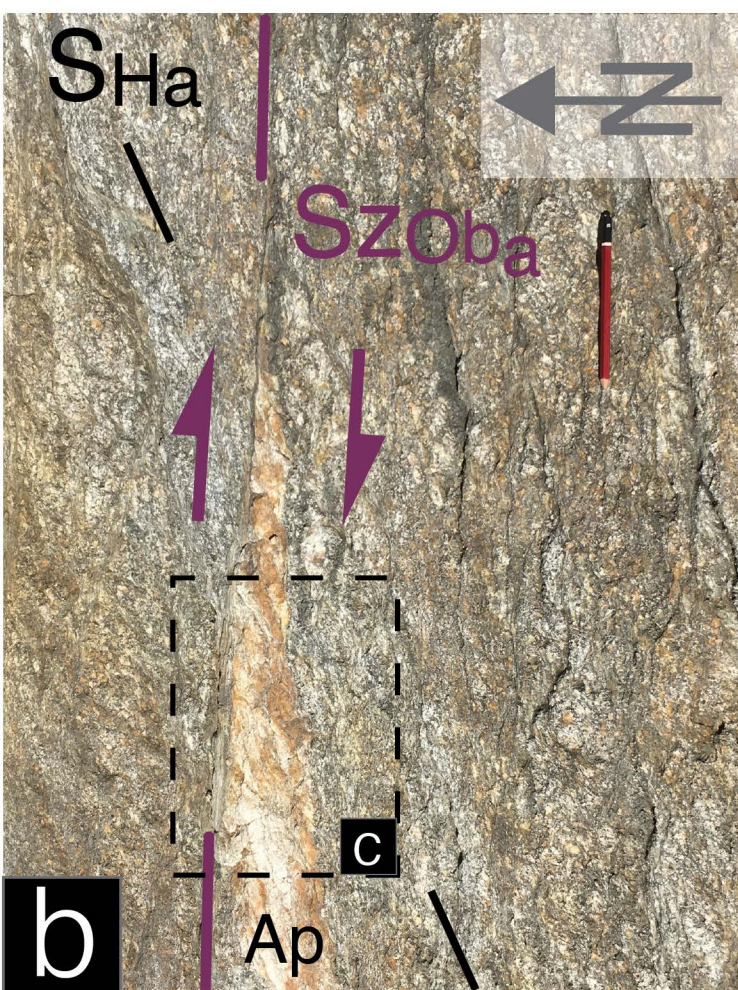
Supplementary Fig. B



Supplementary Fig. C



**a**

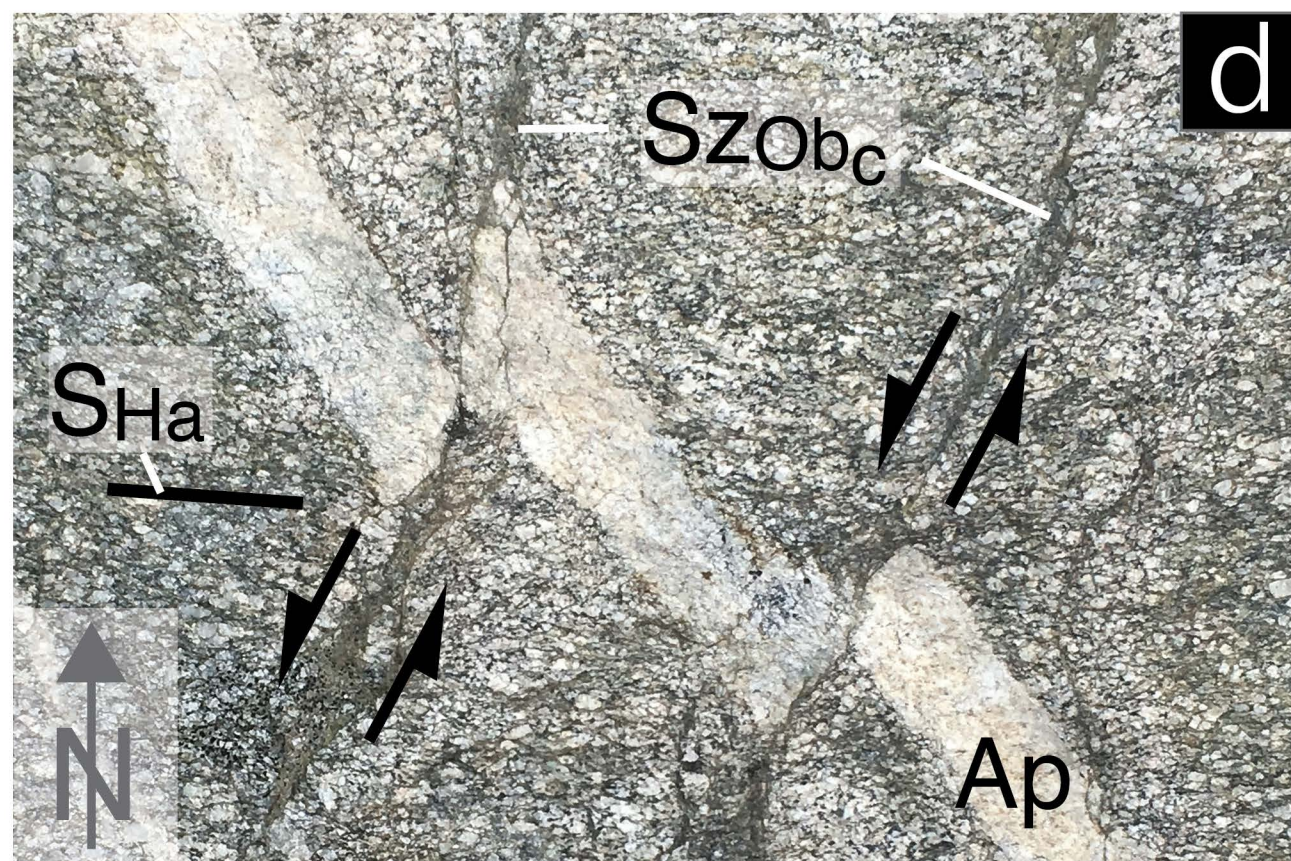
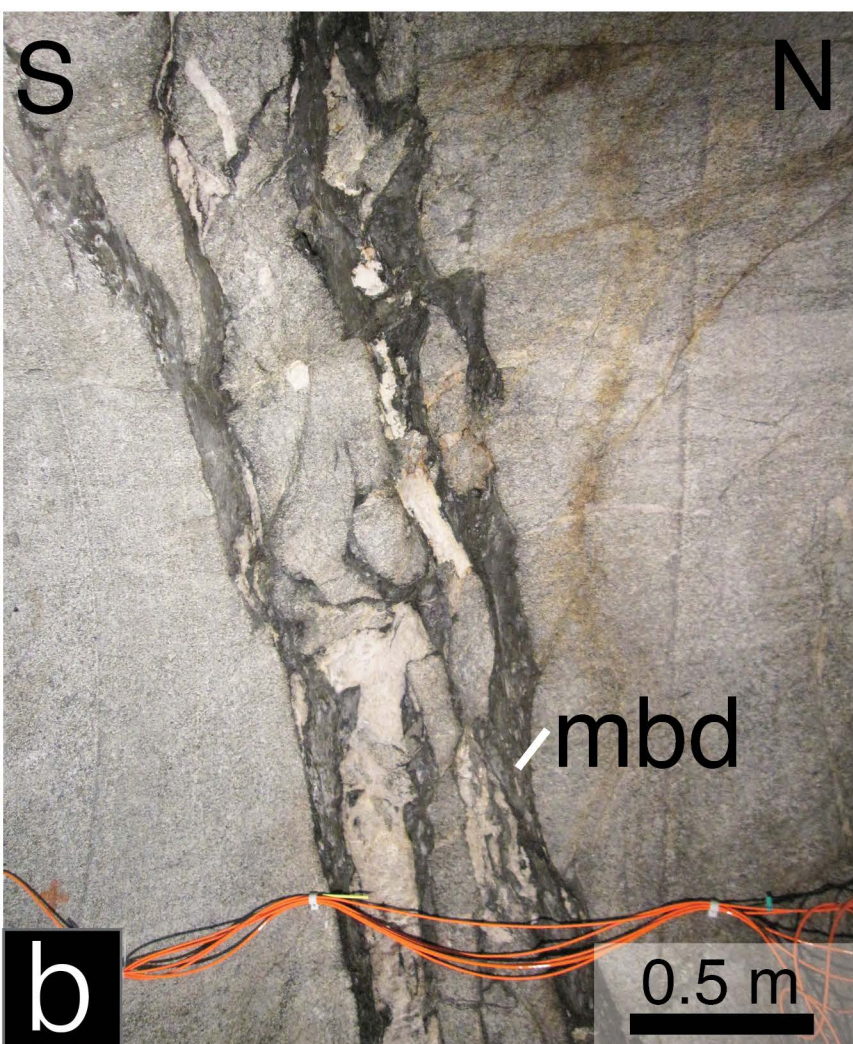
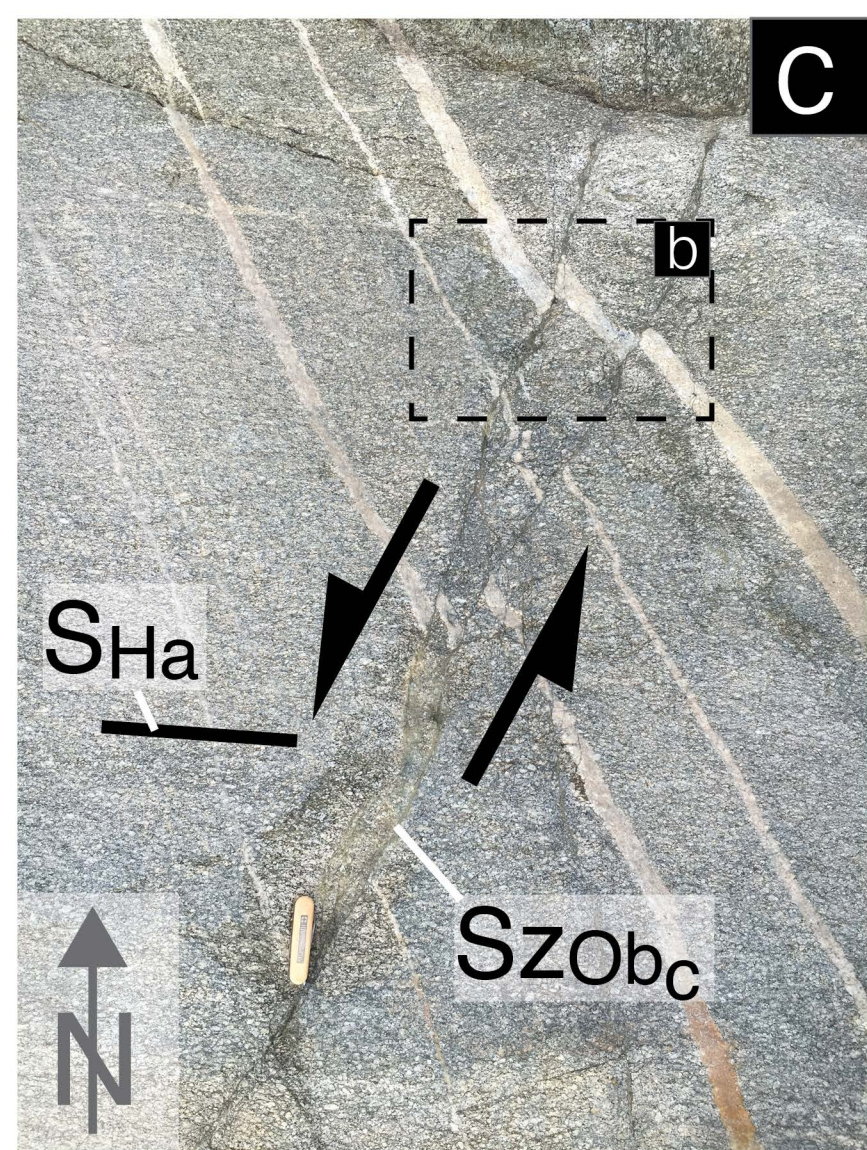
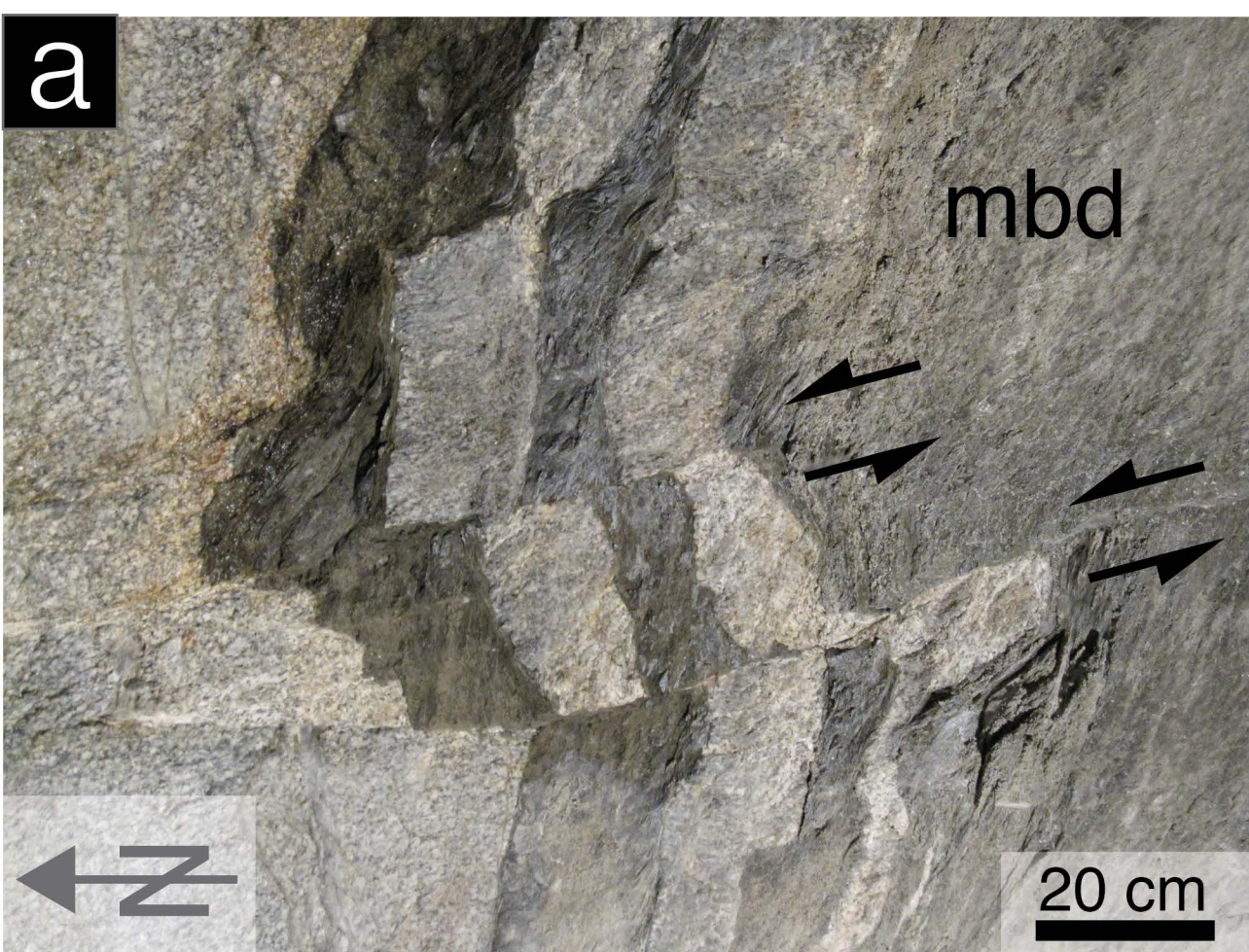


**b**



**c**

Supplementary Fig. D



Supplementary Fig. E

